Universitat Ramon Llull

DOCTORAL THESIS

Title	**Drug delivery in photodynamic therapy: From pharmaceutics to animal testing**
Presented by	**María García Díaz**
Centre	**IQS School of engineering**
Department	**Organic Chemistry**
Directed by	**Prof. Santi Nonell Marrugat**
	Prof. Margarita Mora Giménez

C. Claravall, 1-3
08022 Barcelona
Tel. 936 022 200
Fax 936 022 249
E-mail: urlsc@sec.url.es

Chapter 5

Targeted drug delivery systems

Do folate-receptor targeted liposomal photosensitizers enhance photodynamic therapy selectivity?

One of the current goals in photodynamic therapy research is to enhance the selective targeting of tumor cells in order to minimize the risk and the extension of unwanted side-effects caused by normal cell damage. Special attention is given to receptor mediated delivery systems, in particular, to those targeted to folate receptor. Incorporation of a model photosensitizer (ZnTPP) into a folate-targeted liposomal formulation has been shown to lead an uptake by HeLa cells (folate receptor positive cells) 2-fold higher than the non-targeted formulation. As a result, the photocytotoxicity induced by folate-targeted liposomes was improved. This selectivity was completely inhibited with an excess of folic acid present in the cell culture media. Moreover, A549 cells (folate receptor deficient cells) have not shown variations in the liposomal incorporation. Nevertheless, the differences observed were slighter than expected. Both folate-targeted and non-targeted liposomes localize in acidic lysosomes, which confirms that the non-specific adsorptive pathway is also involved. These results are consistent with the singlet oxygen kinetics measured in living cells treated with both liposomal formulations.

5.1. INTRODUCTION

One of the most actively pursued goals in photodynamic therapy (PDT) research is to enhance the selective targeting of tumor cells in order to minimize the risk and extension of unwanted side-effects caused by damage to normal tissues [1]. Targeted drug delivery systems are one of the strategies proposed to solve the problems underlying traditional cancer treatments. Drug delivery systems are able to modify the pharmacokinetics and biodistribution of their associated drugs. In this way, liposomes possess many interesting properties such as the ability to entrap both hydrophilic and hydrophobic drug molecules without loss or alteration of their activity, long systemic circulation times, preferential accumulation in solid tumors, and controlled drug release [2-4]. In PDT, it has been shown that liposomes increase the photosensitizing efficiency of some PDT agents by maintaining their monomeric form, by modifying the uptake of the dye by malignant cells, or by influencing their subcellular accumulation [5,6].

One approach to improve the therapeutic efficacy of drug-carrying liposomes is the grafting of tumor-specific ligands to their lipid bilayer, which can be recognized by specific cell surface components [7], e.g., antibodies [8], growth factors [9], glycoproteins (transferrin) [10], or specific receptors [11]. The incorporation of ligand-targeted therapies not only facilitates targeting to the cell but also drug retention at the target site by preventing the rapid elimination from the system circulation. These ligands represent a minimal risk of inducing immune response, are widely available and often inexpensive. At present, special attention is given to folate receptor (FR)-mediated delivery systems [12]. Folic acid is an essential vitamin for the proliferation and maintenance of all cells. The lack of this nutrient in human serum makes malignant cells to up-regulate this receptor to compete more aggressively for the vitamin. The overexpression of folate receptor on a variety of epithelial cancer cells including cancers of ovary, lung, kidney, breast, brain and colon [13], and the extremely high affinity of folate for its receptor provide a novel approach to specifically deliver photosensitizers (PSs) encapsulated in folate-functionalized liposomes *in vitro* [14]. Improved uptake of PS-folate conjugates has been reported previously [15,16] and different systemic carrier platforms have been developed to achieve selective accumulation of PSs [17-21]. However, the details of such improved PS uptake are poorly understood. For instance, to what extent does receptor-mediated uptake affect the accumulation of PSs in the cells? Does receptor-mediated uptake affect the localization of the PSs in the cells? Are the photosensitization properties affected?

In order to address these questions, the model PS zinc-tetraphenylporphyrin (ZnTPP) was encapsulated in folate-targeted and non-targeted liposomes to assess the role of folate receptors in the active uptake of folate-targeted liposomes. ZnTPP was chosen as PS as it can be conveniently encapsulated in liposomes in high yield and in monomeric state   [22,23]. Our results show that targeting HeLa cells (FR-overexpressing cervical carcinoma cell line) with folate-decorated liposomes indeed leads to an increased PS uptake. This enhancement induces higher photodynamic cell death compared to that caused by incubation with non-targeted liposomes. We subsequently describe a comparative study of accumulation and phototoxicity in FR-expressing HeLa tumor cells, and in A549 tumor cells which do not express FR. Subcellular localization patterns of both formulations were studied, as well as $^1O_2$ kinetics measured in living cells.

5.2. EXPERIMENTAL SECTION

Materials. 1-palmitoyl-2-oleoyl-*sn*-glycero-3-phosphocholine (POPC), 1,2-dioleoyl-*sn*-glycero-3-[phospho-*L*-serine] (sodium salt) (OOPS) and 1,2-distearoyl-*sn*-glycero-3-phosphoethanolamine-N-[folate(polyethylene glycol)-2000] (ammonium salt) (FA-PEG-DSPE) were purchased from Avanti Polar Lipids (Birmingham, AL). Imidazole, folic acid and 5,10,15,20-tetraphenyl-21*H*,23*H*-porphine zinc (ZnTPP) was purchased from Sigma-Aldrich Chemical Co. (St. Louis, MO) The porphyrin used had a minimal purity of 99% and was used as received. Deuterium oxide (99.9%) was purchased from Solvents Documentation Synthesis (SDS, Peypin, France). All other chemicals were commercially available reagents of at least analytical grade. Milli-Q water (Millipore Bedford, Massachusetts system, resistivity of 18 M□ cm) was used.

Light source. Irradiation was carried out with a Sorisa Photocare LED source with a wavelength range of 520-550 nm. The light intensity at the irradiation site was 16 mW/cm^2, measured with a LaserStar Ophir power meter (Logan, UT).

Cell cultures. Human HeLa cervical adenocarcinoma cell line (ATCC CCL-2) is one of many tumor cell types that are known to over-express folate receptors [24]. Human lung adenocarcinoma A549 cells (ATCC CCL-185), known to be deficient in FR expression, were used as negative control. Before the experiments the cells were subcultured in folate-deficient DMEM (FD-DMEM) supplemented with the same components as DMEM for 2 weeks to establish a folate deficiency.

Preparation of liposomes. POPC/OOPS (90:10 molar ratio, non-targeted liposomes) and POPC/OOPS/FA-PEG-DSPE (90:10:0.1 molar ratio, FR-targeted liposomes) were prepared by microemulsification, following standard procedures. A concentration of 100:1 lipid/porphyrin molar ratio was used.

Cellular internalization. In order to study the liposome cell internalization [25] and to distinguish surface bound to internalized liposomes, HeLa cells were incubated either at 4ºC (where folate-receptor-mediated endocytosis is blocked [14,26]) or 37ºC in the

dark for 4 h with FD-DMEM containing 10 μM ZnTPP encapsulated in non-targeted and FR-targeted liposomes. Since folate rapidly dissociates from specific, high-affinity binding factors in acid pH [27], we used an acidic saline wash to remove surface-bound liposomes and distinguish the uptake due to surface binding than that due to internalization. After rising with PBS, cells were incubated for 10 min with acetate buffer pH 3.5 (130 mM NaCl, 20 mM NaAc). Cells were then scrapped and resuspended in 1 mL of 2% SDS. The extent of PS uptake was assessed by the same procedure described in chapter 2.

Subcellular localization quantitative analysis. Quantitative studies on HeLa cells subjected to 1 or 10 μM ZnTPP in liposomes with and without folate were carried out using image processing and analysis (IPA) from the public domain ImageJ 1.42 software (http://rsbweb.nih.gov/ij/index.html) [28]. The red ZnTPP signal was recorded for each cell, brightness values in arbitrary units corresponding to the following ratio: integrated density/area. Results were the mean values and standard deviations from a total of 70 images. In addition, the frequency of brightness values (red signal) was also evaluated for cells subjected to 24 h treatments with 1 or 10 μM ZnTPP in liposomes either with or without folate.

Statistical analysis. Unpaired Student's *t* test was used to test for the significance level between two sets of measurements. The level of significance was set to $p < 0.05$.

5.3. RESULTS AND DISCUSSION

Characterization of liposomal formulations. FR-targeted and non-targeted liposomes containing ZnTPP at 100:1 lipid/porphyrin molar ratio were prepared by microemulsification. This particular combination of PS and lipids allows for a high encapsulation of this PS [22]. The PS encapsulation efficacy was close to 90% and was not affected by folate functionalization. Photon Correlation Spectroscopy (PCS) showed a dynamic diameter of 110 nm for non-targeted liposomes and 140 nm for FR-targeted liposomes with a polydispersity index of 0.3. The stability of the formulations was monitored by changes in the particle size and porphyrin and lipid retention over one week storage at 4 ºC in the dark (Table 5.1). The liposomal formulations showed excellent colloidal stability and drug retention during this period. We thus conclude that the properties and stability of liposomal preparations are not affected by the presence of the folate marker.

Table 5.1. Stability of FR-targeted and non-targeted formulations as measured by lipid and PS content, particle size and zeta potential.

Sample	Time (h)	L (%)[a]	P (%)[b]	$Zave/nm$[c]	ζ pot$/mV$[d]
Non-targeted	0	90 ± 2	94 ± 8	110 ± 20	-38 ± 5
	24	97 ± 9	85 ± 10	130 ± 30	-31 ± 3
	168	79 ± 3	83 ± 13	140 ± 20	-30 ± 3
FR-targeted	0	87 ± 4	96 ± 7	140 ± 20	-36 ± 2
	24	97 ± 12	93 ± 4	130 ± 30	-34 ± 2
	168	78 ± 3	83 ± 5	110 ± 20	-35 ± 4

[a] L: Lipid content, expressed as the percentage of lipid in the sample with respect to the lipid present at the initial stage of liposome preparation.

[b] P: Porphyrin content, expressed as the percentage of porphyrin in the sample with respect to the porphyrin present at the initial stage of liposome preparation.

[c] Z average mean.

[d] Zeta potential.

Data are mean values ± SD of at least three independent experiments.

The phase transition temperature of POPC/OOPS (90:10) liposomes was reported previously as -5.1 ± 0.7 °C and was not affected by the incorporation of 1% ZnTPP [22]. Thus, one can reasonably expect that it won't be affected either by the presence of 0.1 mol% FA-PEG-DSPE. The liposomes can therefore be safely assumed to be in the fluid state at 37 °C, temperature at which cell experiments were carried out. In order to ensure that ZnTPP does not escape from liposomes interacting with serum proteins, the stability of liposomes was tested also in the presence of 10% FBS at 37°C. The remaining PS in both FR-targeted and non-targeted liposomal suspensions was always above 90%, indicating that serum proteins do not affect liposome stability and, especially, do not induce the release of the entrapped ZnTPP.

The same holds true for the photophysical properties of the sensitizer: Fig. 5.1 shows the absorption and emission spectra of ZnTPP encapsulated in folate-targeted liposomes and their non-targeted counterparts. No spectral shifts can be observed between the two sets of data, ruling out any significant interaction of the porphyrin with the folate ligand. Likewise, the fluorescence quantum yield of ZnTPP, calculated by steady-state comparative method of optically-matched solutions, was 0.025 and 0.024 for folate-targeted liposomes and non-targeted liposomes, respectively ($\Phi_{F\ (ZnTPP,\ toluene)}$ = 0.033) [29]. Finally, the fluorescence decay kinetics, determined by time-correlated single photon counting, also confirmed that the photophysics of ZnTPP in the lipid bilayers are
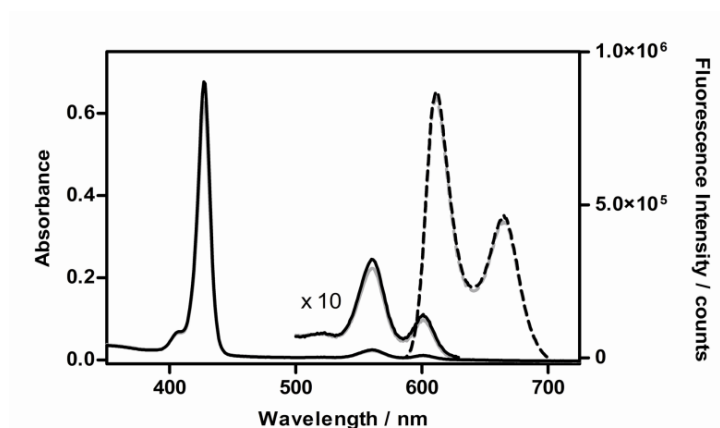

Figure 5.1. Absorption (solid line) and emission (dashed line) spectra of ZnTPP incorporated in folate-targeted liposomes (black) and non-targeted liposomes (grey) in 50 mM imidazole-HCl buffer, pH 7.4. Note the factor x10 in the 500-650 nm region of absorption spectra. The spectra were corrected relative to absorption at 550 nm.

not affected by the presence of the FA-PEG-DSPE ligand. The fluorescence decay could be fitted in both systems by two exponential components with lifetimes 2.0 ± 0.1 and 1.3 ± 0.1 ns, respectively, reflecting different endoliposomal locations of ZnTPP in the phospholipid bilayer [30].

Cellular uptake of FR-targeted liposomes. After confirming that ZnTPP incorporation into the lipid bilayers is not affected by the presence of the FA-PEG-DSPE ligand, the effect of the folate marker on the cellular uptake of ZnTPP was determined. To select the ZnTPP concentration in cell cultures for uptake experiments, the PS dark toxicity was determined after incubation with 1 - 50 μM ZnTPP for up to 24 h. Cell viability was evaluated 24 h after treatment by the MTT colorimetric assay. A concentration of 10 μM ZnTPP was chosen as a good compromise between cell viability and PS concentration in culture medium, with survivals fractions higher than 85% for non-targeted and folate-targeted formulations, for both cell lines.

HeLa and A549 cells were incubated for different times with 10 μM ZnTPP encapsulated in folate-targeted and non-targeted liposomes. The extent of PS uptake was then determined by fluorescence spectroscopy after lysing the cells and then normalized to the protein content of each sample to correct for variations in the number of cells. As shown in Fig. 5.2A, a clear differential uptake between folate-targeted and non-targeted liposomes was observed. Thus, when FR-overexpressing HeLa cells were incubated for 24 h with folate-targeted liposomes, a 70% increase of lysate fluorescence is observed compared to the values for non-targeted liposomes. Moreover, FR-deficient A549 cells showed no differences in the liposomal incorporation (Fig. 5.2B). These results confirm that active uptake mediated by folate receptors is an effective approach to increase the uptake of PS encapsulated in folate-functionalized liposomes.

Additional evidence for the specific role of folate-receptor interactions in the differential uptake of ZnTPP was obtained from competitive binding assays. Thus, 1 mM folic acid was added to the incubation medium to saturate the receptors on the cell surface. Fig. 5.3 shows that 1 mM free folic acid significantly reduced the ZnTPP uptake in HeLa cells targeted with liposomes bearing folate ligands and no differences were observed between targeted and non-targeted liposomes uptake, indicating that the contribution of folate receptors to the uptake of ZnTPP was completely inhibited.
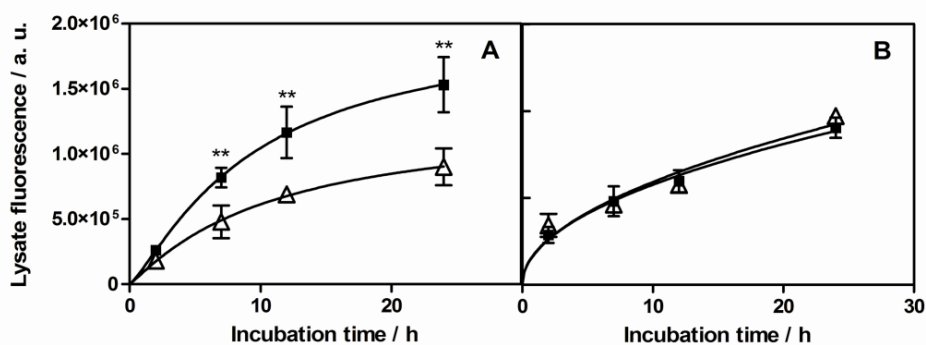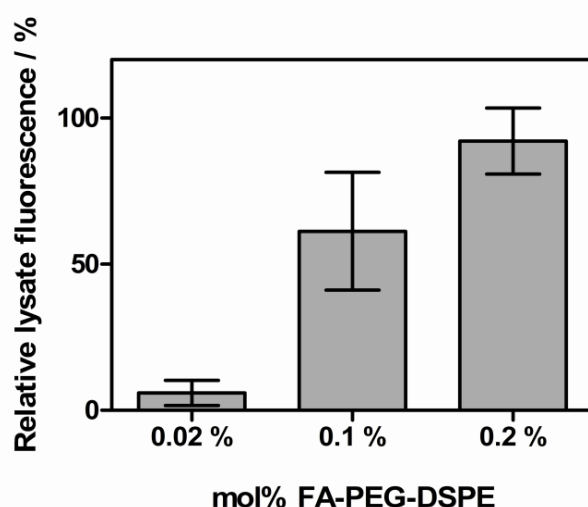
Figure 5.2. Cellular uptake of ZnTPP encapsulated in folate-targeted liposomes (■) and non-targeted liposomes (△) by (A) HeLa and (B) A549 cells in folate-depleted DMEM media. The fluorescence change plotted is the ratio between the area under the fluorescence emission and the protein content in each suspension. Mean ± SD values from at least two different experiments are shown. ** $p < 0.01$
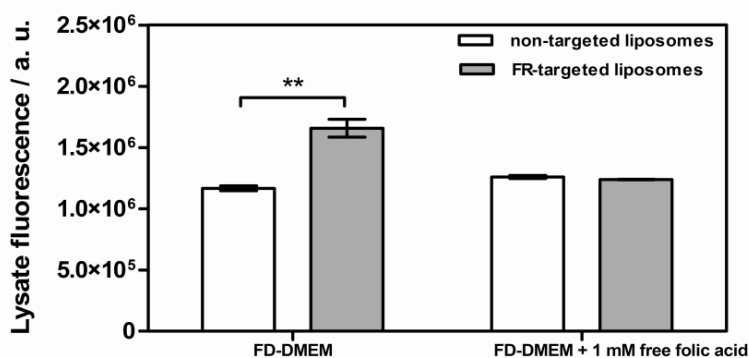
Figure 5.3. Competitive binding assay in HeLa cells cultured with FR-targeted and non-targeted liposomes, with or without the addition of 1 mM free folic acid. The enhancement of the FR-targeted liposomes uptake was totally inhibited in the presence of 1 mM free folic acid. Fluorescence emission was normalized with protein content of each suspension. Mean ± SD values from at least two different experiments are shown. ** $p < 0.01$.

In a third series of experiments, the effect of FA-PEG-DSPE liposomal content on the uptake of ZnTPP was also assessed. HeLa cells were incubated for 24 h with different formulations containing 0 - 0.2 mol% of FA-PEG-DSPE and the fluorescence of the cell lysate was measured and normalized to the protein content of each sample. As expected, uptake of ZnTPP was found to be notably dependent on the amount of FA-

PEG-DSPE present in the liposomes (Fig. 5.4). Increasing amounts of the folate ligand led to higher uptake of the PS although saturation effects were observed at the highest FA-PEG-DSPE concentration assayed. Since FR can bind only one molecule of folic acid [27], we chose to use 0.1 mol% FA-PEG-DSPE in all experiments, which also precludes the formation of folate dimers and trimers [31]. Thus, we can ensure an efficient interaction with folate receptors.

Figure 5.4. Uptake of ZnTPP encapsulated in folate-targeted formulations with varying percentages of FA-PEG-DSPE by HeLa cells. Cells were incubated for 24 hours with non-targeted liposomes (0 mol% FA-PEG-DSPE) or folate-targeted liposomes with the FA-PEG-DSPE mole percentage ranging from 0.02 to 0.2. Fluorescence emission was normalized with protein content of each suspension. The fluorescence emission plotted is relative to the lysate fluorescence of cells treated with non-targeted liposomes. The lysate fluorescence corresponding to 0 mol% FA-PEG-DSPE was normalized to 0 ± 12 %. Mean ± SD values from at least three different experiments are shown.

To check whether the incubation at 4°C prevents ZnTPP uptake, the cell-surface binding capacity of folate-targeted and non-targeted liposomes was estimated from the differential uptake of ZnTPP by HeLa cells incubated at 4°C or 37°C (Fig. 5.5). In both cases, the extent of PS uptake was dramatically reduced when the incubation of ZnTTP-containing liposomes was performed at 4°C, suggesting that endocytosis is the main cell internalization mechanism. Moreover, at this low temperature, almost a two-fold increase of cell-lysate fluorescence was observed for folate-targeted liposomes compared to non-targeted ones. This indicates that the differential uptake between folate-targeted and non-targeted liposomes is amplified due to enhanced surface

binding of the former. Nevertheless, an acidic wash of the cells caused the release of surface-bound folate-targeted liposomes, showing that the uptake due to binding to the folate receptor was greatly diminished under such acidic conditions [14].
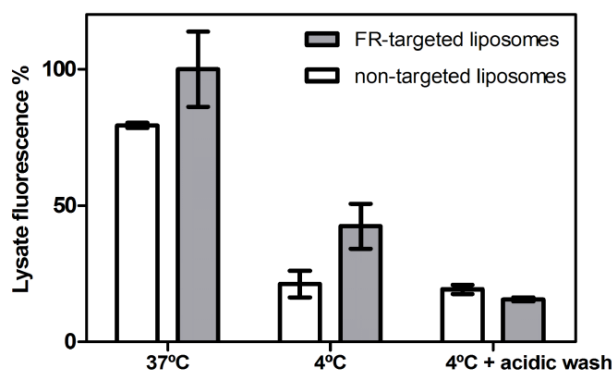

Figure 5.5. Temperature-dependent uptake of ZnTPP encapsulated in folate-targeted and non-targeted liposomes. Cells were incubated for 4 hours at 37°C or 4°C. The cells were then washed with cold PBS or with acidic saline buffer to remove unattached liposomes or either stripped of surface-bound liposomes. Fluorescence emission was normalized with protein content of each suspension. The fluorescence emission plotted is relative to the mean lysate fluorescence of cells treated with folate-targeted liposomes at 37°C, normalized to 100 ± 14 %. Mean ± SD values from at least three different experiments are shown.

Taking all these results together, the preferential uptake of folate-targeted liposomes was demonstrated in HeLa cells. Nevertheless, the differences observed were smaller than expected [14,32,33]. Moreover, non-targeted liposomes are also internalized, revealing that non-specific endocytosis also contribute to the uptake. Qualls and Thompson [17] also observed non-specific liposomal uptake pathways when KB cells, also overexpressing folate receptors [14], were treated with $AlPcS_4^{4-}$ encapsulated in folate-displasmenylcholine liposomes.

Photosensitization experiments. Studies on the efficiency of the FR-targeted liposomes for PDT are summarized in Figs. 5.6 and 5.7. A549 and HeLa cells were incubated in the dark with different concentrations of ZnTPP entrapped in FR-targeted and non-targeted liposomes for 24 h prior to photosensitization. Afterwards, cells were exposed to green light using a LED source. Cell survival was assessed by MTT assay 24 h after treatment. Dark cytotoxicity experiments yielding survival cell fraction higher

than 85% demonstrated that incubation with FR-targeted and non-targeted liposomes at the concentrations used did not induce significant cell death without irradiation. Fig. 5.6 shows the light and concentration dependence of the photodynamic response of HeLa cells for both types of ZnTPP-loaded liposomes. As expected, increasing the light dose and the concentration of the PS led to enhanced photocytotoxicity. Folate-decorated liposomes consistently led to higher photosensitivity of the cells. Irradiation of cell cultures alone or incubated with empty liposomes did not induce any toxicity.
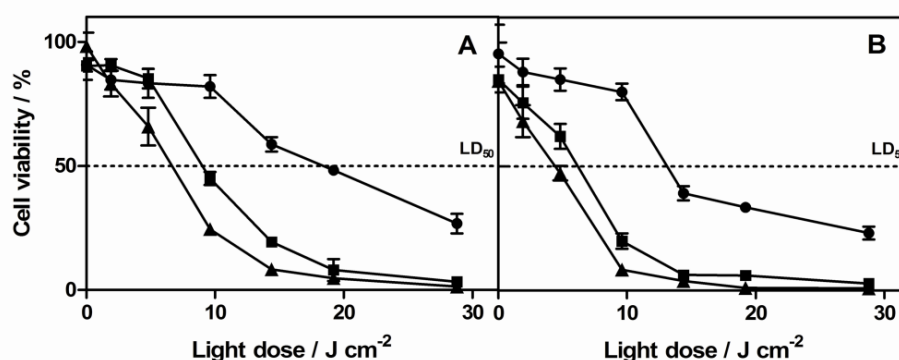
Figure 5.6. Concentration and irradiation time dependence of photocytotoxicity of ZnTPP encapsulated in (A) non-targeted liposomes and (B) folate-targeted liposomes by HeLa cells. The concentrations represented are (●) 0.1 μM , (■) 1 μM and (▲) 10 μM. Mean ± SD from at least three different experiments are shown.

A better appreciation of the folate-labeling effects can be gained by comparing the photodynamic effect under the same conditions. Thus, for 1 μM ZnTPP incubated for 24 h in A549 and HeLa cells and irradiated with 10 J·cm^{-2} (Fig. 5.7), non-targeted liposomes caused 65 ± 5% cell death in both cell lines. The use of FR-targeted liposomes increased the cell mortality to 94 ± 5% for FR-positive HeLa cells, while it remained at 60 ± 5% for FR-negative A549 cells. Thus folate-targeted liposomes enhanced cell mortality by 50% in FR-positive HeLa cells.
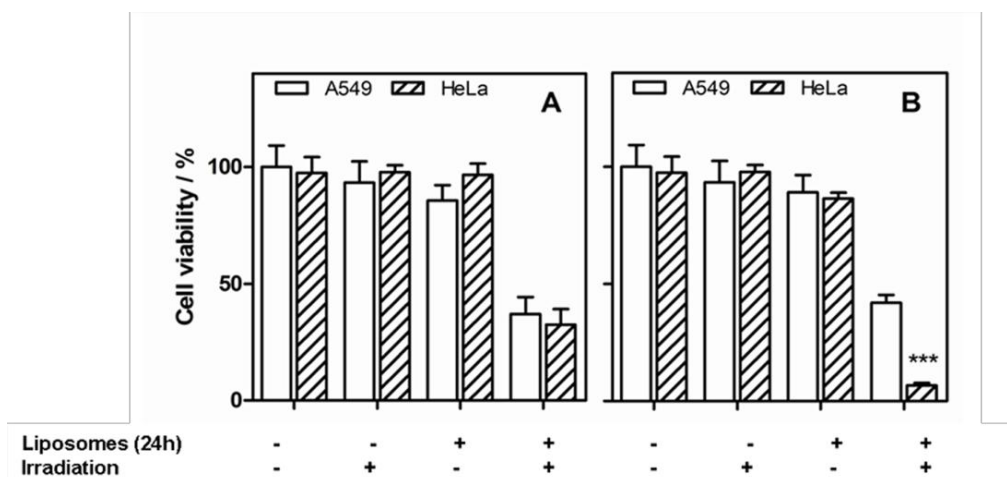
Figure 5.7. Photodynamic induced citotoxicity of ZnTPP encapsulated in (A) non-targeted liposomes and (B) folate-targeted liposomes (1 μM, 10 J/cm^2). Mean ± SD from at least three different experiments are shown. ****p < 0.001*

Subcellular localization. Fluorescence and differential interference contrast images of HeLa cells after 24 or 48 h incubation with folate-targeted and non-targeted liposomes (10 μM ZnTPP bulk concentration) are shown in Fig. 5.8. The cells displayed a pattern of intense granular signal in the cytoplasm. The site of ZnTPP accumulation strongly resembled that of acidic organelles and therefore, lysosomes could be the main site of ZnTPP accumulation. Additionally, the intracellular localization of ZnTPP was compared with the distribution of fluorescent probes specific to lysosomes (LysoTracker Red) and to mitochondria (MitoTracker Red). LysoTracker and Mitotracker Red probes are commonly used in several research areas, including PDT studies [34,35]. As shown in Fig. 5.8A, the intracellular distribution of ZnTPP was clearly similar to LysoTracker Red, and clearly different from the mitochondrial network displayed with MitoTracker Red, under green excitation epifluorescence microscopy. We could not observe the co-localization of ZnTPP and LysoTracker probe because of the red emission of both dyes. The intensity of the punctate fluorescence was dependent on the porphyrin concentration, incubation time, as well as ZnTPP liposomal formulation. It is important to note that no morphological changes were detected in the cells under these conditions and no relocalization of the PS was observed when cells were exposed to prolonged exciting light. Non-specific adsorptive endocytosis pathway was confirmed by the fact that the intracellular localization of ZnTPP from by non-targeted liposomes was identical to that of liposomes with folate.

Cells treated with 10 µM ZnTPP vehiculized in liposomes with folate appeared with a higher fluorescence signal in relation to folate-free liposomes (see Fig. 5.8A). These results were confirmed by the quantitative analysis of fluorescence intensity using ImageJ 1.42 software (Fig. 5.8B and C), and results are consistent with the cellular uptake measured by cell lysate fluorescence.
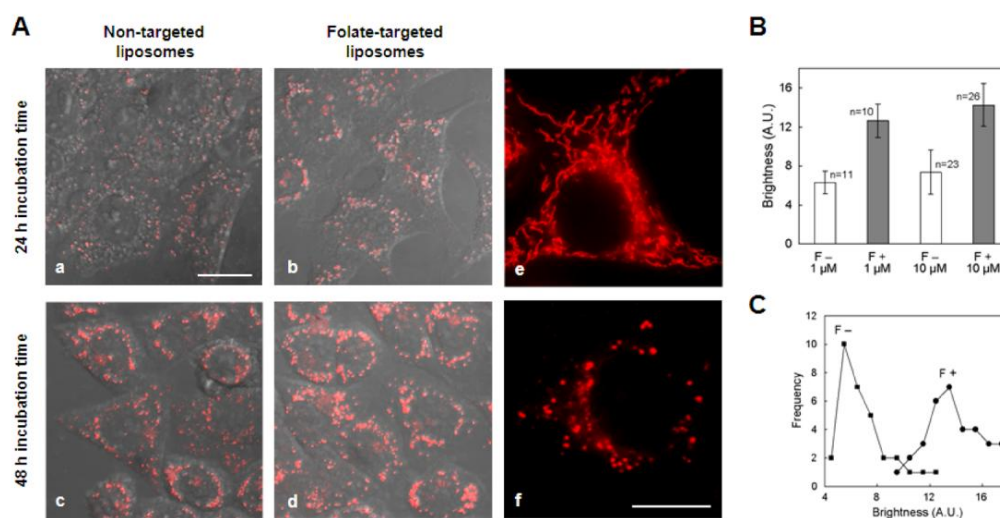

Figure 5.8. A) Confocal microscopy images of living HeLa cells incubated 24 or 48 h with different liposomal formulations of 10 µM ZnTPP. (a) and (b) Subcellular localization of ZnTPP in HeLa cells incubated 24 h in liposomes without and with folate, respectively. (c) and (d) Cells displaying the fluorescence pattern of ZnTPP 48 h after incubation in liposomes without and with folate, respectively. All images are the overlay of the fuorescence signal and differential interference contrast (DIC). Scale bar: 10 µm. (e) Localization of MitoTracker Red in HeLa control cells. (f) Localization of LysoTracker Red in HeLa control cells. B) and C) Microscopical evaluation of ZnTPP uptake. B: Mean brightness values (± SD) of the signal from HeLa cells treated for 24 h with 1 or 10 µM ZnTPP in liposomes with (F+) or without (F-) folate. C: Distribution of brightness values from HeLa cells subjected to 24 h treatments with both 1 and 10 µM ZnTPP in liposomes either with or without folate.

Time-resolved $^1O_2$ detection in HeLa cells incubated with ZnTPP encapsulated in FR-targeted and non-targeted liposomes. In a typical experiment, 1.5 mL- D_2O-based PBS (D-PBS) cell suspension containing ~ 8 x 10^6 cells incubated with ZnTPP encapsulated in FR-targeted and non-targeted liposomes was assayed for $^1O_2$ using pulsed laser excitation at 532 nm and observing the $^1O_2$ phosphorescence at 1280 nm. Indeed, the samples produced clear $^1O_2$ phosphorescence signals showing the expected rise-and-decay shape (Fig. 5.9). Kinetic analysis of the data in Fig. 5.9

yielded lifetimes $\tau_1 = 1.5 \pm 0.4$ μs for the rise and $\tau_2 = 6.0 \pm 0.5$ μs for the decay, the same results being obtained for both FR-targeted and non-targeted liposomes. Thus, the kinetics of $^1O_2$ production and decay in HeLa cells are not affected by the presence of folate ligands on the surface of the liposomes used for delivery of the ZnTPP, suggesting a similar final localization of the PS, in agreement with the confocal microscopy results.
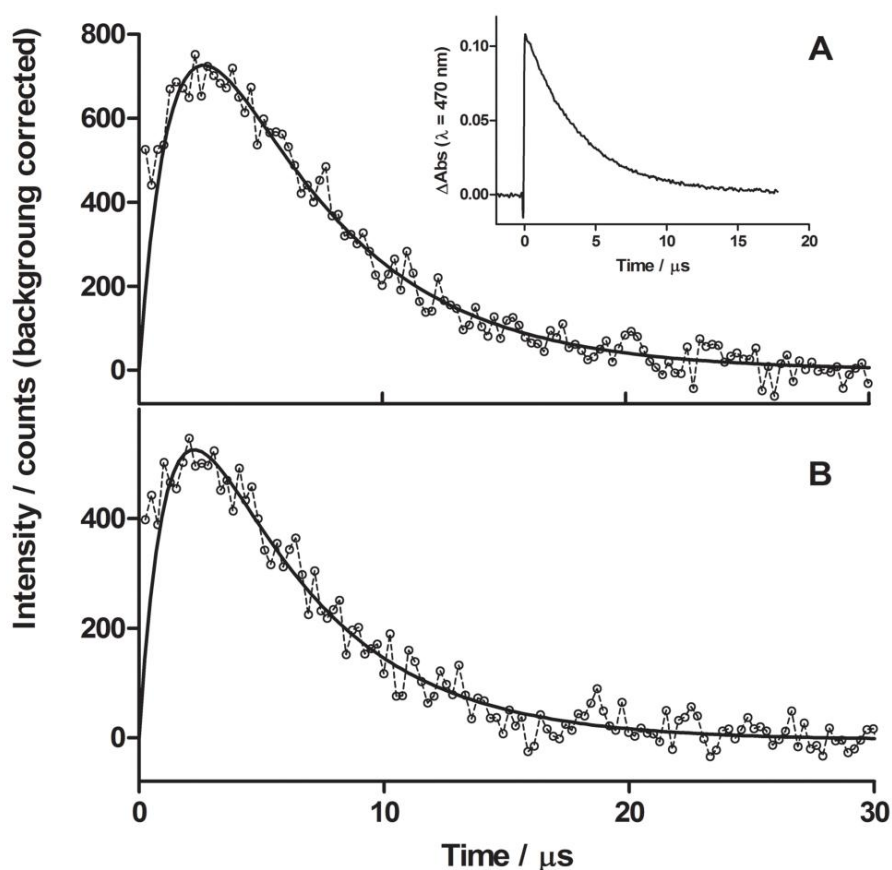
Figure 5.9. Time-resolved luminescence decays of $^1O_2$ recorded at 1280 nm upon 532 nm excitation of a D-PBS HeLa cell suspension, previously incubated with 10 μM ZnTPP encapsulated in (A) non-targeted and (B) folate-targeted liposomes during 24 h in the dark. A: fitted parameters: $\tau_1 = 1.5 \pm 0.4$ μs, $\tau_2 = 5.8 \pm 0.5$ μs ; Inset A: ΔAbs signal recorded at 470 nm (triplet absorption), fitted parameters: $\tau_1 = 5 \pm 1$ μs; B: fitted parameters: $\tau_1 = 1.5 \pm 0.4$ μs, $\tau_2 = 6.1 \pm 0.5$ μs.

The inset in Fig. 5.9A shows the transient absorbance of ^{3}ZnTPP in the cell suspension. Kinetic analysis of this signal yields $\tau_T = 5 \pm 1$ μs, which means that $\tau_\Delta = 1.5 \pm 0.4$ μs in HeLa cells. This lifetime is much shorter than the typical value in D_2O (60-70 μs, [36]) indicating that $^1O_2$ is substantially quenched in these cells. Given diffusion coefficients of singlet oxygen in the 0.4 - 2 x 10^{-5} cm^2 s^{-1} range [37-39] and the typical size of the lysosomes (50-500 nm), it can be safely concluded that primary $^1O_2$ damage will be confined to this organelle, as found previously in human skin fibroblasts [40]. Indeed, we were not able to quench $^1O_2$ with standard quenchers such as sodium azide or bovine serum albumin.

5.4. CONCLUSIONS

A novel folate-targeted liposomal formulation of the model PS ZnTPP has been developed for its selective delivery to FR-overexpressing cancer cells. The stability of liposomal formulations and the photophysical properties of the PS are not affected by the presence of the folate ligand. This folate-targeted formulation shows enhanced ZnTPP internalization and phototoxicity by folate-receptor-positive cells, although non-specific pathways are also involved in cellular uptake. Confocal microscopy and $^1O_2$ kinetics measured in living cells indicate a lysosome localization of ZnTPP in HeLa cells, irrespective of the presence of folate on the liposome surface.

The prevention of liposome uptake at low temperature accounts for the involvement of endocytic pathways in the cellular internalization of both targeted and non-targeted liposomes. Moreover, the reduction of ZnTPP fluorescence in the cells' lysates after an acidic wash confirms the interaction of the folate-targeted liposomes with the receptors. These observations are consistent with the lysosomal localization of ZnTPP.

Taken together, our results suggest that folate ligands enhance the cellular uptake in FR-positive cells mainly as a result of a sustained contact between the liposome and the cell surface, thereby increasing the liposomes' ability to internalize drugs. It will be interesting to see whether in cells with higher FR overexpression this folate-induced selectivity can be further increased. In addition, it will be interesting to study the efficacy of FR-targeted liposomes in preclinical models and their potential for future clinical application in photodynamic therapy.

5.5. REFERENCES

[1] W.M. Sharman, J.E.V. Lier, C.M. Allen. Targeted photodynamic therapy via receptor mediated delivery systems, Adv. Drug Deliv. Rev. 56 (2004) 53-76.

[2] A.S. Derycke, P.A.d. Witte. Liposomes for photodynamic therapy, Adv. Drug Deliv. Rev. 56 (2004) 17-30.

[3] T.L. Andresen, S.S. Jensen, K. Jorgensen. Advanced strategies in liposomal cancer therapy: problems and prospects of active and tumor specific drug release, Prog. Lipid Res. 44 (2005) 68-97.

[4] D.K. Chatterjee, L.S. Fong, Y. Zhang. Nanoparticles in photodynamic therapy: an emerging paradigm, Adv. Drug Deliv. Rev. 60 (2008) 1627-1637.

[5] X. Damoiseau, H.J. Schuitmaker, J.W. Lagerberg, M. Hoebeke. Increase of the photosensitizing efficiency of the Bacteriochlorin a by liposome-incorporation, J. Photochem. Photobiol.B: Biol. 60 (2001) 50-60.

[6] M.C. Galanou, T.A. Theodossiou, D. Tsiourvas, Z. Sideratou, C.M. Paleos. Interactive transport, subcellular relocation and enhanced phototoxicity of hypericin encapsulated in guanidinylated liposomes via molecular recognition, Photochem. Photobiol. 84 (2008) 1073-1083.

[7] A.A. Gabizon, H. Shmeeda, S. Zalipsky. Pros and cons of the liposome platform in cancer drug targeting, J. Liposome Res. 16 (2006) 175-183.

[8] K. Maruyama, O. Ishida, T. Takizawa, K. Moribe. Possibility of active targeting to tumor tissues with liposomes, Adv. Drug Deliv. Rev. 40 (1999) 89-102.

[9] A. Gijsens, L. Missiaen, W. Merlevede, P.d. Witte. Epidermal growth factor-mediated targeting of chlorin e6 selectively potentiates its photodynamic activity, Cancer Res. 60 (2000) 2197-2202.

[10] M. Singh. Transferrin As A targeting ligand for liposomes and anticancer drugs, Curr. Pharm. Des. 5 (1999) 443-451.

[11] P. Sapra, T.M. Allen. Ligand-targeted liposomal anticancer drugs, Prog. Lipid Res. 42 (2003) 439-462.

[12] W. Xia, P.S. Low. Folate-Targeted Therapies for Cancer, J. Med. Chem. 53 (2010) 6811-6824.

[13] N. Parker, M.J. Turk, E. Westrick, J.D. Lewis, P.S. Low, C.P. Leamon. Folate receptor expression in carcinomas and normal tissues determined by a quantitative radioligand binding assay, Anal. Biochem. 338 (2005) 284-293.

[14] R.J. Lee, P.S. Low. Delivery of liposomes into cultured KB cells via folate receptor-mediated endocytosis, J. Biol. Chem. 269 (1994) 3198-3204.

[15] R. Schneider, F. Schmitt, C. Frochot, Y. Fort, N. Lourette, F. Guillemin, et al. Design, synthesis, and biological evaluation of folic acid targeted tetraphenylporphyrin as novel photosensitizers for selective photodynamic therapy, Bioorg. Med. Chem. 13 (2005) 2799-2808.

[16] J. Gravier, R. Schneider, C. Frochot, T. Bastogne, F. Schmitt, J. Didelon, et al. Improvement of meta-tetra(hydroxyphenyl)chlorin-like photosensitizer selectivity with folate-based targeted delivery. synthesis and in vivo delivery studies, J. Med. Chem. 51 (2008) 3867-3877.

[17] M.M. Qualls, D.H. Thompson. Chloroaluminum phthalocyanine tetrasulfonate delivered via acid-labile diplasmenylcholine-folate liposomes: intracellular localization and synergistic phototoxicity, Int. J. Cancer 93 (2001) 384-392.

[18] R. Hudson, R.W. Boyle. Strategies for selective delivery of photodynamic sensitisers to biological targets, J. Porphyrins Phthalocyanines. 8 (2004) 954-975.

[19] D. Bechet, P. Couleaud, C. Frochot, M.L. Viriot, F. Guillemin, M. Barberi-Heyob. Nanoparticles as vehicles for delivery of photodynamic therapy agents, Trends Biotechnol. 26 (2008) 612-621.

[20] K. Stefflova, H. Li, J. Chen, G. Zheng. Peptide-based pharmacomodulation of a cancer-targeted optical imaging and photodynamic therapy agent, Bioconjug. Chem. 18 (2007) 379-388.

[21] B.C. Bae, K. Na. Self-quenching polysaccharide-based nanogels of pullulan/folate-photosensitizer conjugates for photodynamic therapy, Biomaterials 31 (2010) 6325-6335.

[22] F. Postigo, M. Mora, M.A. De Madariaga, S. Nonell, M.L. Sagrista. Incorporation of hydrophobic porphyrins into liposomes: characterization and structural requirements, Int. J. Pharm. 278 (2004) 239-254.

[23] F. Postigo, M.L. Sagrista, M.A. De Madariaga, S. Nonell, M. Mora. Photosensitization of skin fibroblasts and HeLa cells by three chlorin derivatives: Role of chemical structure and delivery vehicle, Biochim. Biophys. Acta. 1758 (2006) 583-596.

[24] C.P. Leamon, P.S. Low. Membrane folate-binding proteins are responsible for folate-protein conjugate endocytosis into cultured cells, Biochem. J. 291 (Pt 3) (1993) 855-860.

[25] H. Hillaireau, P. Couvreur. Nanocarriers' entry into the cell: relevance to drug delivery, Cell Mol. Life Sci. 66 (2009) 2873-2896.

[26] C.P. Leamon, P.S. Low. Delivery of macromolecules into living cells: a method that exploits folate receptor endocytosis, Proc. Natl. Acad. Sci. U.S.A. 88 (1991) 5572-5576.

[27] B.A. Kamen, A. Capdevila. Receptor-mediated folate accumulation is regulated by the cellular folate content, Proc. Natl. Acad. Sci. U.S.A. 83 (1986) 5983-5987.

[28] M. Alvarez, A. Villanueva, P. Acedo, M. Canete, J.C. Stockert. Cell death causes relocalization of photosensitizing fluorescent probes, Acta Histochem. (2010).

[29] J.P. Strachan, S. Gentemann, J. Seth, W.A. Kalsbeck, J.S. Lindsey, D. Holten, et al. Effects of orbital ordering on electronic communication in multiporphyrin arrays, J. Am. Chem. Soc. 119 (1997) 11191-11201.

[30] F. Ricchelli, G. Jori. Distribution of porphyrins in the various compartments of unilamellar liposomes of dipalmitoyl-phosphatidylcholine as probed by fluorescence spectroscopy, Photochem. Photobiol. 44 (1986) 151-157.

[31] F. Ciuchi, G. Dinicola, H. Franz, G. Gottarelli, P. Mariani, M.G.P. Bossi, et al. Self-Recognition and Self-Assembly of Folic-Acid Salts - Columnar Liquid-Crystalline Polymorphism and the Column Growth-Process, J. Am. Chem. Soc. 116 (1994) 7064-7071.

[32] J.M. Saul, A. Annapragada, J.V. Natarajan, R.V. Bellamkonda. Controlled targeting of liposomal doxorubicin via the folate receptor in vitro, J. Control. Released 92 (2003) 49-67.

[33] J. Wu, Q. Liu, R.J. Lee. A folate receptor-targeted liposomal formulation for paclitaxel, Int. J. Pharm. 316 (2006) 148-153.

[34] N.S. Trivedi, H.W. Wang, A.L. Nieminen, N.L. Oleinick, J.A. Izatt. Quantitative analysis of Pc 4 localization in mouse lymphoma (LY-R) cells via double-label confocal fluorescence microscopy, Photochem. Photobiol. 71 (2000) 634-639.

[35] J.A. Caruso, P.A. Mathieu, J.J. Reiners. Sphingomyelins suppress the targeted disruption of lysosomes/endosomes by the photosensitizer NPe6 during photodynamic therapy, Biochem. J. 392 (2005) 325-334.

[36] P.R. Ogilby, C.S. Foote. Chemistry of Singlet Oxygen. 42. Effect of Solvent, SolventIsotopic Substitution, and Temperature on the Lifetime ofSinglet Molecular Oxygen (1Ag), J. Am. Chem. Soc. 105 (1983) 3423.

[37] J. Moan. On the diffusion length of singlet oxygen in cells and tissues, J. Photochem. Photobiol. B:Biol. 6 (1990) 343-347.

[38] E. Skovsen, J.W. Snyder, J.D.C. Lambert, P.R. Ogilby. Lifetime and diffusion of singlet oxygen in a cell, J. Phys. Chem. B. 109 (2005) 8570-8573.

[39] S. Hackbarth, J. Schlothauer, A. Preuss, B. Roder. New insights to primary photodynamic effects--Singlet oxygen kinetics in living cells, J. Photochem. Photobiol. B:Biol. 98 (2010) 173-179.

[40] A. Jimenez-Banzo, M.L. Sagrista, M. Mora, S. Nonell. Kinetics of singlet oxygen photosensitization in human skin fibroblasts, Free Radic. Biol. Med. 44 (2008) 1926-1934.

Chapter 6
Photodynamic therapy *in vivo*

Antitumor photodynamic therapy of temocene: the role of formulation and targeting strategy

In this chapter, the novel photosensitizer temocene was tested for its photodynamic therapy (PDT) effectiveness against the P815 tumor, both *in vitro* and in DBA/2 tumor bearing mice. The effects of the drug delivery system on its PDT activity, localization and tumor accumulation were investigated. Temocene was administered either free (dissolved in PEG_{400}/EtOH mixture), or encapsulated in Cremophor EL micelles, or in DPPC/DMPG liposomes. The maximum cell accumulation and photodynamic activity *in vitro* was achieved with the free photosensitizer, while temocene in Cremophor micelles hardly entered the cells. Notwithstanding, the micellar formulation showed the best *in vivo* response when used in a vascular regimen (short drug light interval), whereas liposomes were found to be an efficient drug delivery system for a tumor cell targeting strategy (long drug-light interval). PEG/EtOH formulation could not be used for *in vivo* experiments due to toxic effects caused by photosensitizer aggregation. These results confirmed that both formulation and targeting strategy are crucial determinants of PDT response of a photosensitizer.

6.1. INTRODUCTION

There are three main mechanisms that operate to allow photodynamic therapy (PDT) to destroy tumors: 1) direct cellular killing by necrosis and/or apoptosis [1-3], 2) tumor-associated vascular damage leading to thrombosis and hemorrhage that subsequently cause tumor hypoxia [4-6], and 3) activation of antitumor immune response contributing to tumor destruction even in distant locations [7-9]. It is generally accepted that all three mechanisms are necessary for the optimal tumor damage. The relative contribution of these pathways depends upon the photosensitizer (PS) used, the tissue being treated, and treatment conditions. For a particular tissue and PS, the targeting strategy can be modulated by illumination at a short or long interval after drug administration, maximizing vascular or cellular targeting, respectively. The PS is predominantly retained in the tumor vasculature initially after i.v. injection, and light delivery within minutes after administration damages the tumor vasculature [10]. This mechanism has received considerably attention in recent years due to the successful clinical implementations PDT in age-related macular degeneration treatment with verteporfin [11] and prostate cancer treatment with Pd-bacteriochlorophyll derivatives TOOKAD and WST11 [12-14]. Conventional cancer cell targeting approaches allow free diffusion to the PS out into the tissue to be accumulated into the tumor cellular compartment. A long drug-to-light interval generates more direct cytotoxic cellular damage. The selectivity of this strategy relies on the high ratio of drug concentration in the tumor to that in normal surrounding tissue.

Thus, pharmacokinetics of the PS plays an important role in effectiveness of both vascular and cellular PDT. Pharmacokinetics and selectivity can be enhanced by nanoparticles as vehicles for PS delivery. Different approaches have been developed to enable selective accumulation of the PS providing an environment where the PS can be administered in monomeric form and without loss or alteration of its activity [15-18]. Indeed lipid and detergent nanostructures (liposomes and micelles) have been extensively used in PDT. To further investigate these questions, we evaluated the influence of different formulations in PDT effectiveness both *in vitro* and *in vivo*.

The novel PS, temocene [19], was chosen as photoactive molecule in this study. Temocene is the porphycene analogue to *m*-tetrahydroxyphenyl chlorin, commonly named temoporfin. As we have shown in chapter 3, both the photophysical properties and photodynamic activity *in vitro* suggested that temocene was a good candidate for PDT. These results prompted us to further study its effectiveness *in vivo* provided an

effective drug-delivery strategy could be developed for this hydrophobic molecule. Therefore it was either dissolved in PEG_{400}-EtOH mixture, or encapsulated in Cremophor EL micelles or in DPPC/DMPG/PEG_{3000}-DSPE liposomes.

As mentioned above, the targeting strategy is a critical parameter for the success of PDT. Thus, the effects of drug-to-light interval on tumor regression were also investigated. Formulations were administered intravenously and PDT was performed 15 min (vascular targeting) or 24 h (cellular targeting) after injection. We found that Cremophor EL micelles using a vascular targeted short-drug light interval PDT was the best combination for a successful treatment.
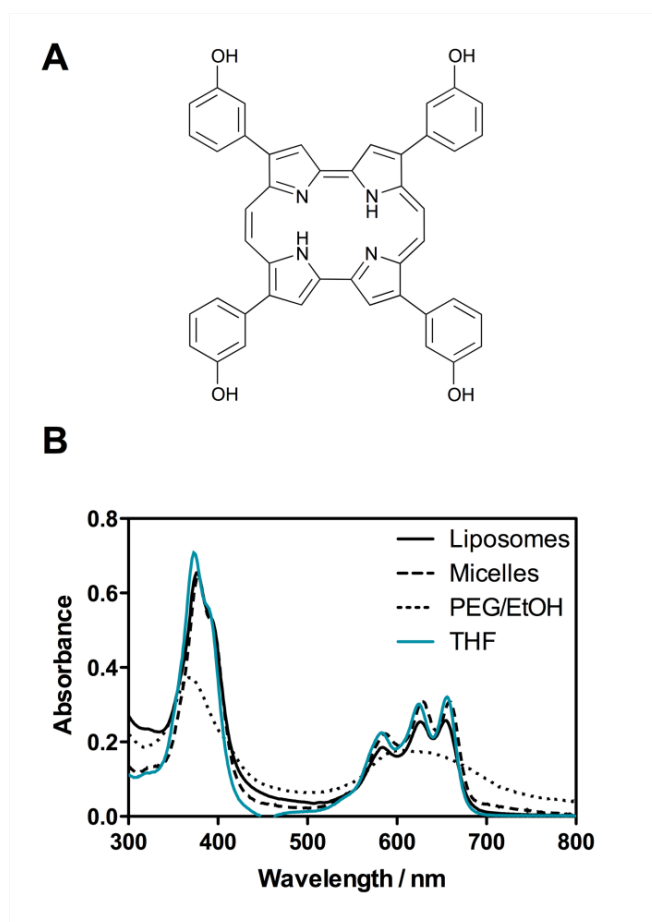
Figure 6.1. A) Chemical structure of temocene. B) Absorption of 2.5 μM temocene in aqueous suspensions of different drug delivery systems: liposomes (black solid line), micelles (dashed line), PEG/EtOH (dotted line). Absorption of temocene dissolved in THF (blue solid line) is shown for comparison.

6.2. EXPERIMENTAL SECTION

Chemicals. The synthesis, molecular characterization and photophysical properties of temocene (Fig. 6.1A) have been previously described in detail (Chapter 3, [19]). For cellular and *in vivo* studies, temocene was dissolved in PEG$_{400}$/EtOH (3:2) or formulated in micelles or liposomes as described in the following sections.

1,2-dipalmitoyl-*sn*-glycero-3-phosphocholine (DPPC), 1,2-dimyristoyl-*sn*-glycero-3-phospho-(1'-rac-glycerol) (DMPG) and 1,2-distearoyl-*sn*-glycero-3-phosphoethanolamine-N-[methoxy(polyethylene glycol)-3000] (*m*-PEG$_{3000}$-DSPE) were purchased from Avanti Polar Lipids (Birminghan, AL). 3-[4,5-dimethylthiazol-2-yl]-2,5-diphenyltetrazolium bromide (MTT), Cremophor EL and Hoechst 33342 were purchased from Sigma-Aldrich Chemical Co. (St. Louis, MO). 3'-(p-hydroxyphenyl) fluorescein (HPF) and Singlet Oxygen Sensor Green (SOSG) were purchased from Molecular Probes (Invitrogen, Carlsbad, CA). MicroBCA protein assay kit was purchased from Pierce Protein Research Products (Rockford, IL) and used according to the product information sheet. All other chemicals were commercially available reagents of at least analytical grade.

Micelle preparation. Cremophor micellar solution was prepared by mixing 1 mg of temocene with 2.5 mL of Cremophor EL solution (100 mg/mL) in dry tetrahydrofuran (THF); 1 mL of THF was added to this mixture. The final Cremophor/temocene ratio was 250:1 (w/w). The resulting solution was stirred until it became one phase and isotropic. The solvent was removed by rotary evaporation. The resulting dry film was completely dissolved in 3 mL of sterile 5% dextrose solution. The micellar suspension was filtered through 0.22 □m mixed cellulose ester filter under sterile conditions to remove unloaded temocene. The encapsulation efficiency was then determined by the ratio of temocene absorbance before and after filtration. The average size and polydispersity of micelles and the zeta potential were determined by photon correlation spectroscopy (PCS). A Zetasizer Nano-ZS (Malvern Instruments, UK) and a 4 mW He-Ne laser (Spectra Physics), at an excitation wavelength of 633 nm, were used.

Liposome preparation. DPPC/DMPG/PEG$_{3000}$-DSPE (67.5:7.5:0.1 molar ratio) mixture containing the porphycene at 75:1 lipid/photosensitizer molar ratio was prepared by microemulsification, following standard procedures described in chapter 2.

Liposomes were lyophilized for enhanced stability during storage and rehydrated just before experiments.

Cell lines. We used both the DBA/2 mastocytoma cell line P815 (ATCC, TIB-64) [20] and the BALB/c colon adenocarcinoma cell line CT26.CL25 (ATCC, CRL-2639) that expressed a tumor antigen, β-galactosidase [21].

Light source. A Lumacare lamp (Newport Beach, CA) fitted with a light guide and a 640-680 nm band-pass filter was used. Light guides were adjusted to give a uniform spot with an irradiance of 20 mW/cm^2 for *in vitro* experiments, and 100 mW/cm^2 for *in vivo* treatments. Light power was measured with a power meter (model DMM 199 with 201 standard head, Coherent, Santa Clara, CA).

Hydroxyl radical and singlet oxygen detection. The fluorescent probes HPF and SOSG (Molecular Probes, Invitrogen) were used to detect hydroxyl radicals and singlet oxygen, respectively. Temocene in the three different delivery systems was added at a final concentration of 5 μM in 100 □L PBS. HPF or SOSG were added to each well at a final concentration of 5 μM. 660-nm light was delivered in sequential doses of 1 J/cm^2. After each dose, the probe fluorescence was measured with a fluorescence plate reader ($\lambda_{exc/em}$ were 490/515 nm for HPF and 504/525 for SOSG). Probes without PS were used as controls to subtract fluorescence due to auto-oxidation of the probe.

Histology studies. Temocene in PEG/EtOH solution was injected in tumor bearing mice (1mg/kg). Lungs, kidneys and liver of dead mice were fixed in 10% formalin and embedded in paraffin using standard histology protocol. Tissue section of 5 μm thickness were cut and stained for H&E according to standard protocol. A glass cover slip was mounted over the specimen using DPX mounting media and the images were analyzed with microscopy (Axiophot, Carl Zeiss Microscopy, Thorwood, NY).

Photobleaching studies during PDT *in vivo.* Temocene in Cremophor EL micelles or DPPC/DMPG liposomes was administered in tumor bearing mice intravenously by tail

vein injection. 24 h after injection 660-nm light was used to irradiate a homogeneous spot of 1.5-cm diameter that covered the tumor and a margin of normal tissue. Mice were imaged with CRI Maestro *in vivo* fluorescence imaging system at different light doses in order to follow the course of photobleaching. After the fluorescence image acquisition, the image cubes were unmixed (deconvolved) using a spectral library containing the autofluorescence of the mice skin and a dilute sample of temocene in the different vehicles.

Statistics. Unpaired Student's *t* test was used to test for the significance level between two sets of measurements and Kaplan-Meier survival curves were compared with a log-rank test using GraphPad Prism version 5.00 for Windows, GraphPad Software, San Diego, CA www.graphpad.com. The level of significance was set to $p < 0.05$.

6.3. RESULTS

Characterization of formulations. In order to compare the effect of the drug delivery system on PDT efficacy, temocene was dissolved in PEG_{400}/EtOH (3:2) or formulated in micelles or liposomes. The absorption spectra of temocene in the different delivery systems are shown in Fig. 6.1B. Dilution in water caused aggregation of temocene dissolved in PEG_{400}/EtOH mixture. Temocene incorporated in Cremophor EL micelles did not show spectral differences compared to THF, so it can be safely assumed that it is in a monomeric state. However, incorporation of temocene into liposomes produced slight changes in its absorption spectrum, namely an intensity decrease of the Soret and Q bands. Similar changes have been observed previously for other PS in liposomes and have been attributed to the ordered lipid environment [22,23].

Table 6.1. Physicochemical characteristics of the different formulations as measured by PS and lipid content, particle size and zeta potential.

Formulation	*PS (%)[a]*	*L (%)[b]*	*Zave/nm[c]*	*ζpot/mV[d]*
Micelles	95 ± 2	n.a.	30 ± 5	-1.5 ± 0.5
Liposomes	90 ± 3	85 ± 5	150 ± 20	-47 ± 2
Liposomes after lyophilization/rehydration	90 ± 5	90 ± 5	180 ± 20	-55 ± 5

Data are mean values ± SD of at least three independent experiments.

[a] %PS: Encapsulation efficiency expressed as the percentage of PS in the sample with respect to the PS present at the initial stage of preparation.

[b] %L: Lipid content, expressed as the percentage of lipid in the sample with respect to the lipid present at the initial stage of liposome preparation.

[c] Z average mean.

[d] Zeta potential.

n.a. not applicable

Table 6.1 summarizes the main features of the different formulations. The encapsulation efficiency of both liposomal and micellar formulation was higher than 90%. However, differences were found regarding the size and the zeta potential. PCS revealed a dynamic diameter of 30 ± 5 nm for micelles, whereas for liposomes it was 150 ± 20 nm. Likewise, the electric potential of the particles surface also differed between the formulations. Specifically, liposomes had a ζ_{pot} of -47 ± 2 mV, due to the phosphatidyl group of DMPG, which gives electrical stability to the colloid formulation.

By contrast, Cremophor micelles had a $\Box$pot close to zero. Despite this fact, the micellar formulation remained stable for several weeks and no flocculation or aggregation phenomena was observed. In this case, the thermodynamic stability came from the steric repulsive forces of the polymer-covered surface. No significant changes in the physicochemical properties were observed after lyophilization/rehydration of liposomes.

Effect of temocene formulation on PDT effectiveness *in vitro.* Studies of the effectiveness of the different temocene formulations are summarized in Fig. 6.2. P815 cells were incubated in the dark with different concentrations of temocene in the three formulations, exposed to red light, and assayed for cell survival. In the in vitro experiments, cells were incubated with different concentrations of temocene during 18 h. There was no dark toxicity in case of liposomal formulation at any of the concentrations tested, whereas the PEG/EtOH solutions showed substantial dark toxicity at high concentrations (Fig. 6.2A). In the presence of light, both formulations showed PDT-induced loss of mitochondrial activity in a concentration-, light dose- and incubation time-dependent manner (Fig. 6.2B, C and D), the PEG/EtOH solution being the most effective at the same concentration and light dose. Interestingly, no PDT effect could be observed with micelles, which showed the same extent of cell kill in the dark as upon delivery of a 3.5 or 10 J/cm^2 light dose. These results are consistent with the uptake studies (Fig. 6.2E) since minimal internalization was observed with the micellar formulation. Specifically, temocene internalization at 24 h was minimum for micelles, maximum for PEG/EtOH, and liposomes showing an intermediate behavior. Notwithstanding the lower uptake, it is worth noting that liposomes are the most effective vehicle when the photodynamic activity is compared on a per-molecule-cell uptake basis (Fig. 6.2F).
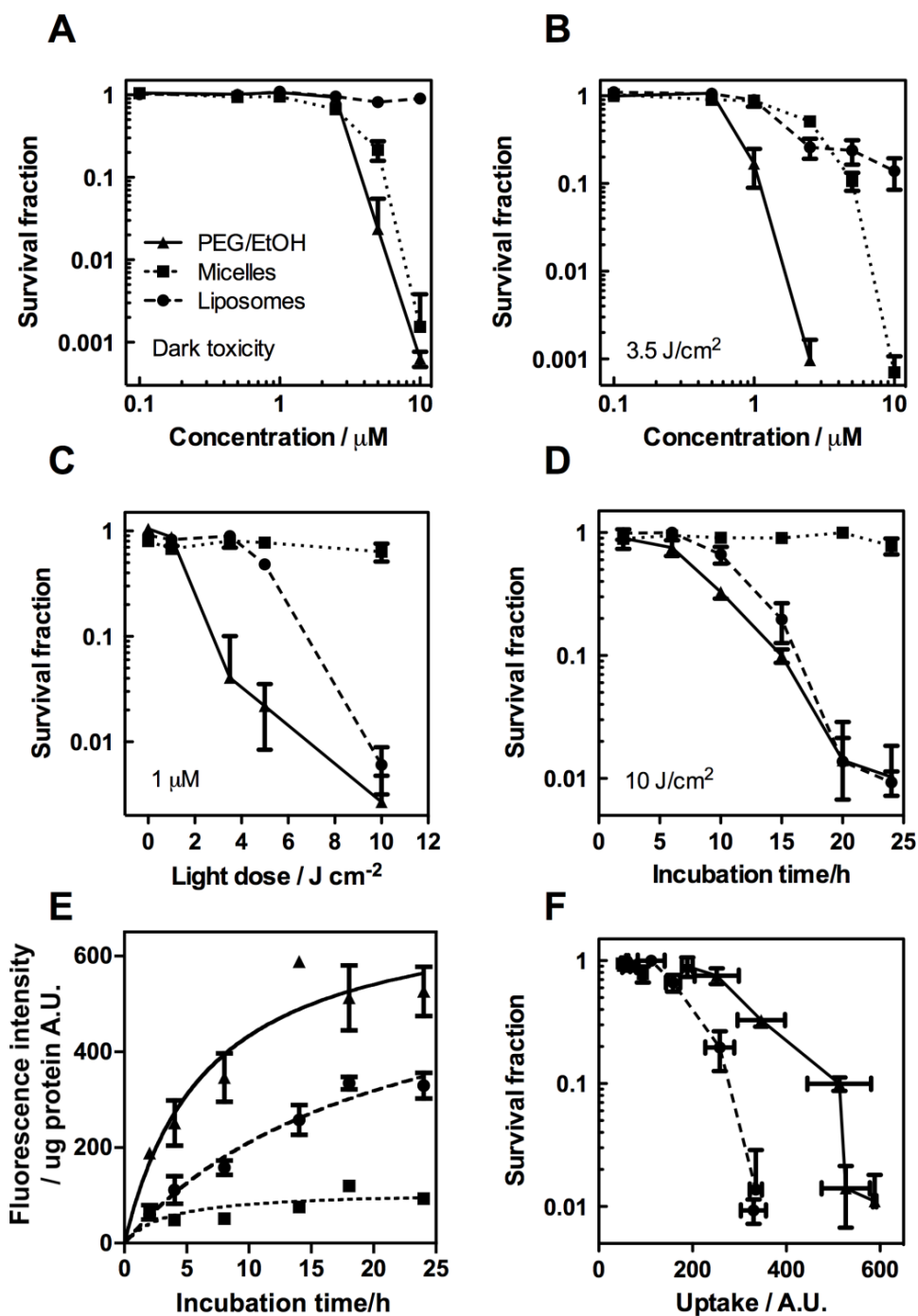
Figure 6.2. *In vitro* PDT effectiveness of temocene dissolved in PEG/EtOH (triangles) or encapsulated in micelles (squares) or liposomes (circles). A) Dark toxicity after 18 h incubation in P815 cell line. B) Effectiveness of 3.5 J/cm^2 after 18 h incubation. C) Light dose dependence after 18 h incubation. D) Effectiveness of 10 J/cm^2 after different incubation times. E) Cellular uptake by P815 cells. F). PDT effectiveness after 10 J/cm^2 per unit uptake.

Subcellular localization. Confocal microscopy was used to examine the intracellular localization of temocene taken up after delivery by the different systems. For these studies the formulations were co-incubated with green-fluorescent probes specific for mitochondria (MitoTracker), lysosomes (LysoTracker) and endoplasmatic reticulum (ER-Tracker). The overlaid images and the fluorescent topographic profiles are shown in Fig. 6.3. The stained patterns of the mitochondrial probe and temocene were different regardless of the formulation, indicating marginal accumulation of the PS in the mitochondria. The fluorescent profile of temocene perfectly matched with the green fluorescence of the lysosomal probe for all formulations. In the case of ER probe, the overlapping was partial. It is important to note that it was necessary to use a higher exposure time for the micrographs of cells incubated with Cremophor micelles due to the limited internalization. No morphological changes were detected in the cells under these conditions and no relocalization of the PS was observed when cells were exposed to confocal excitation light.

Reactive oxygen species production. The ability of temocene to produce different reactive oxygen species (ROS) in the different vehicles was monitored using the fluorescence probes SOSG and HPF. Fig. 6.4 shows that temocene can produce hydroxyl radical as well as singlet oxygen both in micelles and liposomes. Temocene incorporated in micelles was 25% more effective in producing singlet oxygen than in liposomes. However, when incorporated into liposomes it showed a much greater increase in HPF fluorescence in a light dose-dependent manner. These studies indicate that light-dependent effects of temocene incorporated in Cremophor micelles are mainly due to the production of singlet oxygen. The liposomal formulation shows a comparable increase in fluorescence from both HPF and SOSG probes, indicating similar abilities to produce $^1O_2$ and $HO^{\bullet}$. The porphycene dissolved in PEG_{400}/EtOH did not produce any reactive oxygen species, consistent with the extensive aggregation of the PS in aqueous solutions (Fig. 6.1).
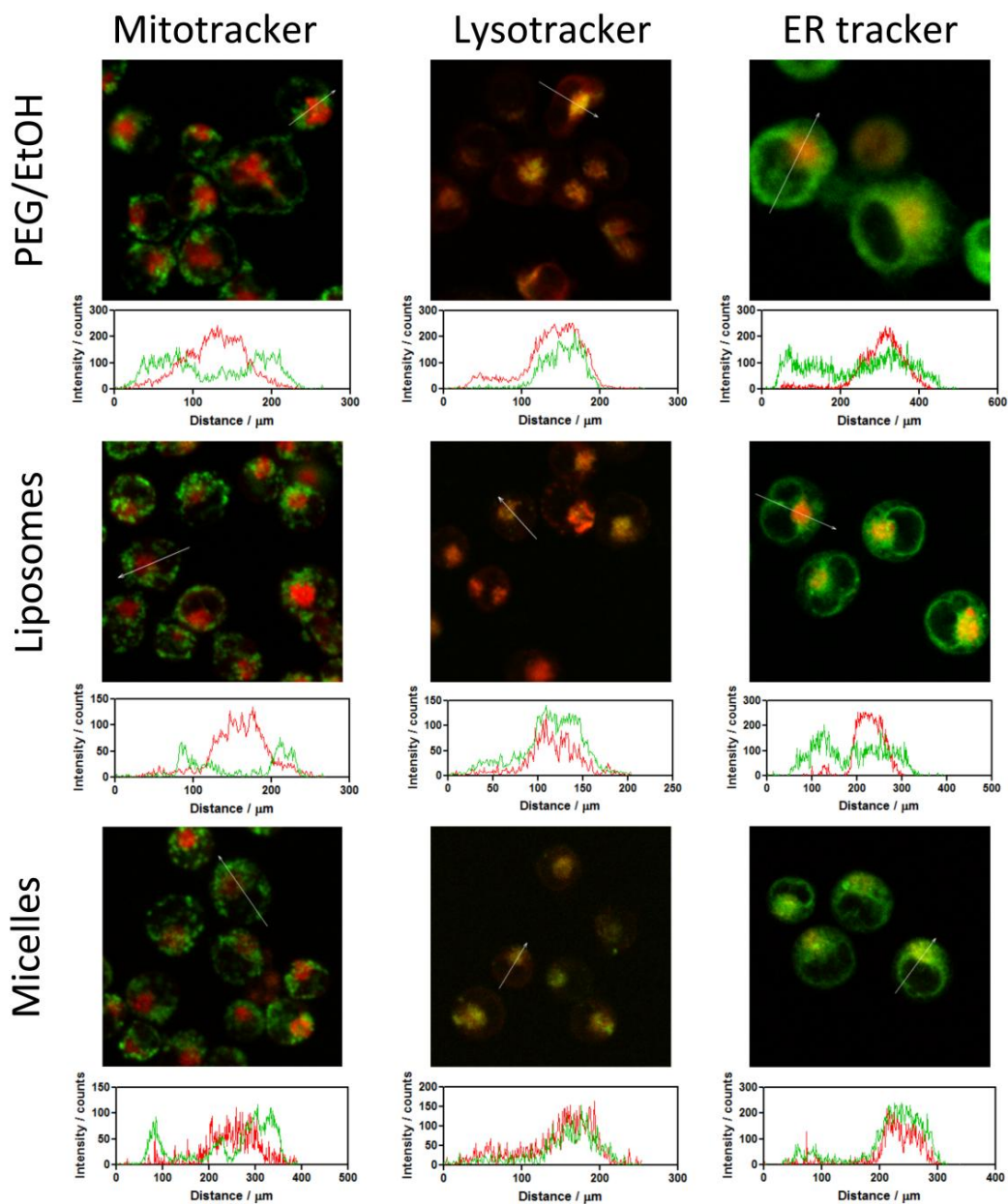
Figure 6.3. Fluorescence micrographs of P815 cells showing red fluorescence from temocene in different formulations overlaid with green fluorescence from lysotracker, mitotracker or ER-tracker. Fluorescent topographic profiles of cells are showed under confocal images. Arrow indicates the analyzed longitudinal transcellular zone.
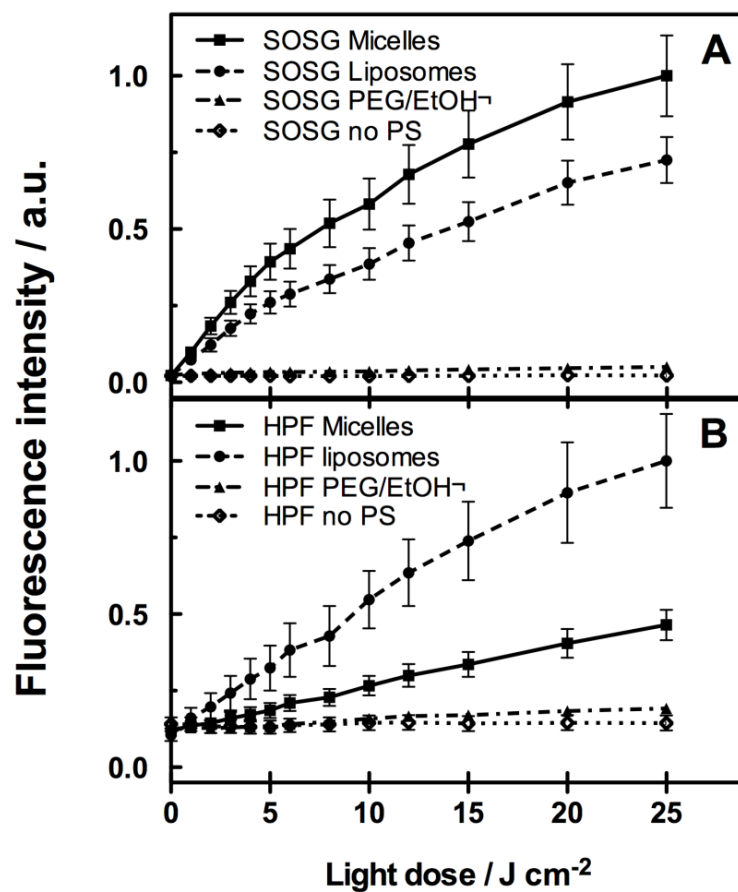
Figure 6.4. Light dose-dependent increase in fluorescence from 5 ꞏM SOSG (A) and HPF (B) in aqueous solution with 5 μM temocene in the different delivery systems.

Effect of temocene formulation on tumor accumulation *in vivo.* Temocene incorporated in PEG/EtOH, micelles or liposomes was injected intravenously through the tail vein in a dose of 1 mg/kg in tumor bearing mice. Temocene dissolved in PEG/EtOH induced death of all the mice immediately after injection because of aggregation of PS in the blood stream that provoked the collapse of lungs and kidneys (see Fig. 6.5). We checked that this toxicity was not due to PEG/EtOH mixture alone (no temocene). The PEG/EtOH formulation was consequently discarded for *in vivo* experiments.
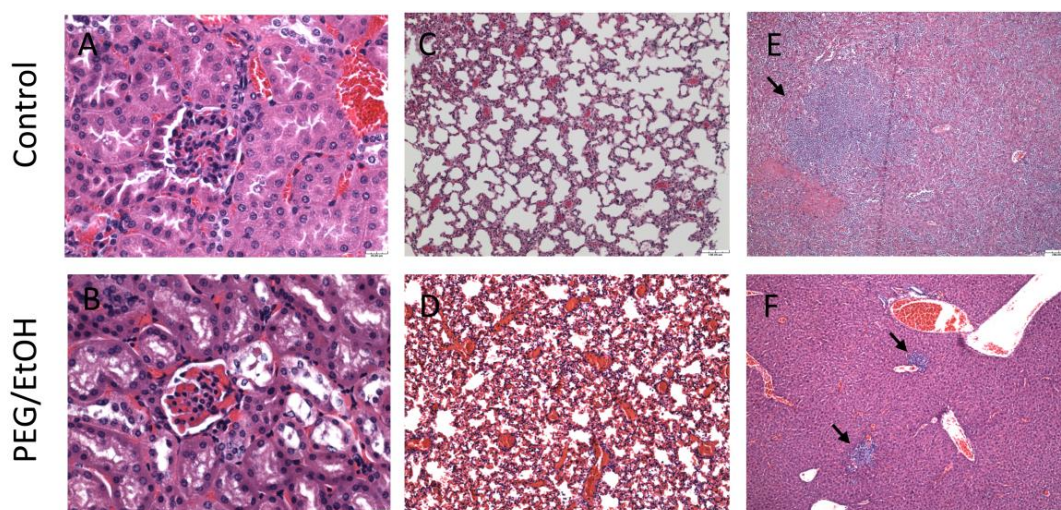
Figure 6.5. H&E histology of tissue sections removed from DBA/2 tumor-bearing mice. Left panels: Control mouse. Right panel: Dead mouse after i.v. injection of temocene dissolved in PEG/EtOH (1 mg/kg). A, B) Kidneys. C, D) Lungs. E, F) Metastatic nodules in liver (arrows)

Collapsed alveoli, thickened interstitial walls, and dense erythrocyte congestion were observed. The collapse of kidneys was also evident. Erythrocyte congestion in the glomerulus is characteristic of intravascular coagulation. We also observed the acute liver metastasis of P815 tumor that caused the death of control mice. In temocene PEG/EtOH injected mice some metastatic nodules are also observed but we can consider that they were not the cause of death.

The tumor accumulation of temocene incorporated in micelles or liposomes was studied by non-invasive methods using a Maestro *in vivo* fluorescence camera system. The results are shown in Fig. 6.6. The pharmacokinetics of tumor uptake was influenced by the drug delivery system. Liposomal temocene showed higher accumulation in the tumor, showing a maximum in fluorescence intensity 24 h after injection. In the case of the micellar formulation, the fluorescence reached its highest intensity 8 h after injection. A high tumor-to-normal tissue ratio for a PS is considered to be important in PDT to ensure the maximum selectivity of the treatment and minimal normal tissue damage. Liposomes showed a better tumor selectivity, accumulating in the tumor three times higher than in the surrounding skin. It is important to note that no significant effect on tumor growth was observed after drug injection (no light, dark control) as compared to absolute control mice (no light and no drug).
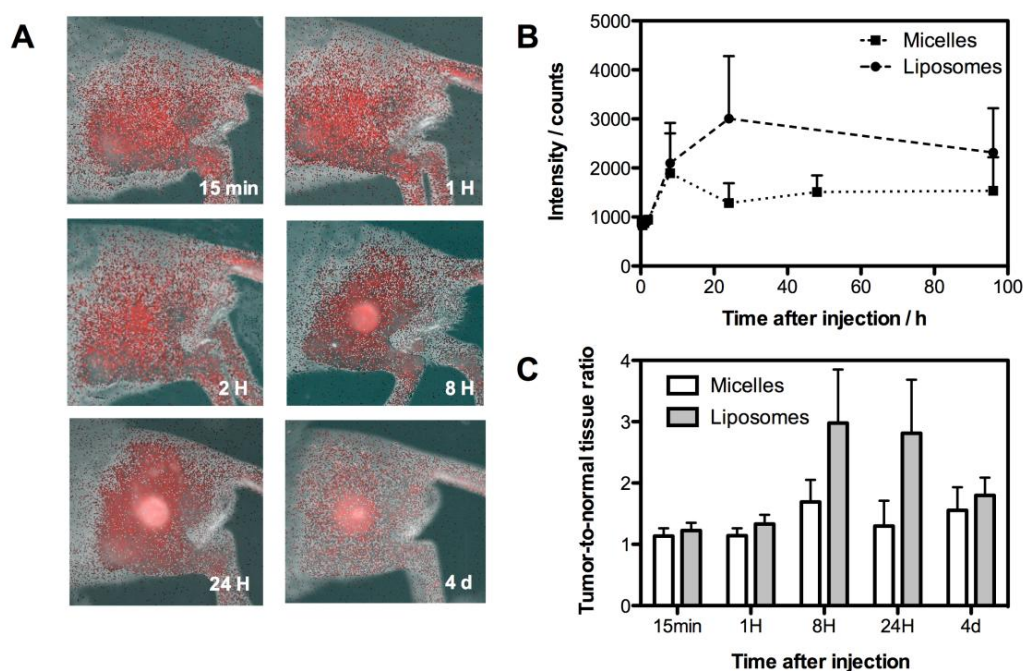
Figure 6.6. Tumor accumulation of temocene incorporated in micelles or liposomes after i.v. injection. A) Series of *in vivo* fluorescence images of temocene encapsulated in liposomes accumulated in P815 tumor. B) Fluorescence intensity of temocene in P815 tumor at different times after i.v. injection. C) Tumor-to-normal tissue ratio calculated by the fraction of the fluorescence intensity in the tumor and the fluorescence intensity in the surrounding skin. Data show the mean ± SD of three mice.

Effect of temocene formulation and targeting strategy on PDT effectiveness *in vivo.* Tumor bearing mice were divided into the following groups and each group included 8-10 animals:

- control groups: dark control (no light), light control (no drug), absolute control (no light and no drug)

- vascular response group: mice treated with 150 J/cm^2 15 min after i.v. injection of 1 mg/kg liposomal or micellar temocene.

- cellular response group: mice treated with 150 J/cm^2 24 h after i.v. injection of 1 mg/kg liposomal or micellar temocene.

Mean tumor volumes plot and Kaplan-Meier survival analysis are shown in Fig. 6.7. In all cases, PDT produced a local response in P815-treated tumors, as manifested by an acute inflammation and edema in the first 24 h after treatment followed by tumor necrosis and a dark eschar formation over the area formerly occupied by the tumor. Subsequently a marked reduction in tumor size was observed. Animals were observed for up to 60 days after treatment for metastasis development, tumor regrowth and tissue healing. No significant differences in survival or tumor volume progress were observed between the different control groups so we only plotted absolute controls for the sake of clarity.

The combined therapy of micellar formulation with short drug-to-light interval was clearly the most effective combination. This group resulted in a total regression of the principal tumor and stayed in remission for the whole course of observation (Fig. 6.7A). It is important to note that although P815 grew as localized subcutaneous tumors, they also metastasized to draining lymph nodes and liver fairly early in the course of disease [24,25], so the complete regression of principal tumor does not consequently imply the animal survival. In this case, temocene encapsulated in micelles resulted in a delay or even avoidance (3 out of 8 mice) of metastasis (Fig. 6.7C). The vascular PDT regime using the liposomal formulation of temocene was not highly effective resulting in a local tumor regrowth relatively quickly. In marked contrast was the cellular targeting strategy (Fig. 6.7B and D), liposomal treatment led to a delay of tumor regrowth and a significant survival advantage. PDT performed 24 hours after injection of temocene in Cremophor micelles had no effect in terms of survival compared to controls and local tumor regrew few days after treatment.
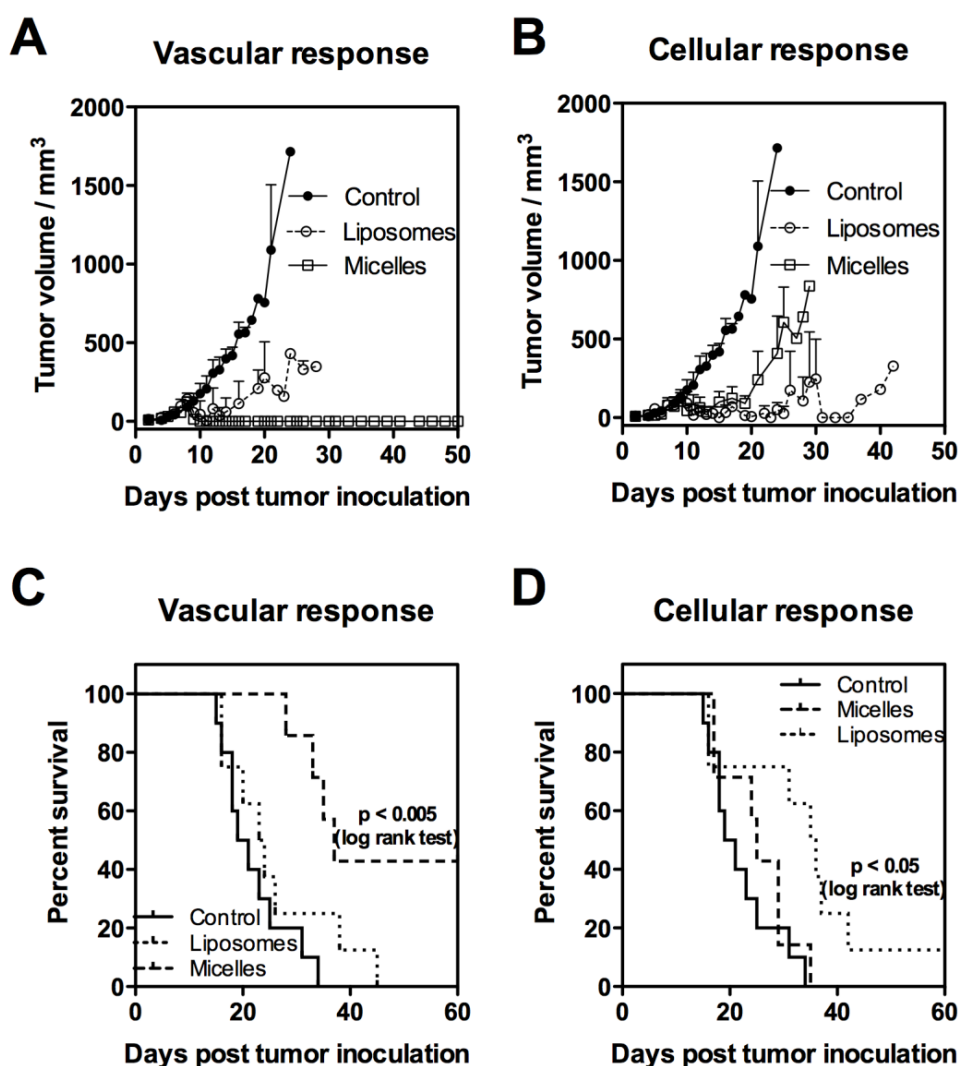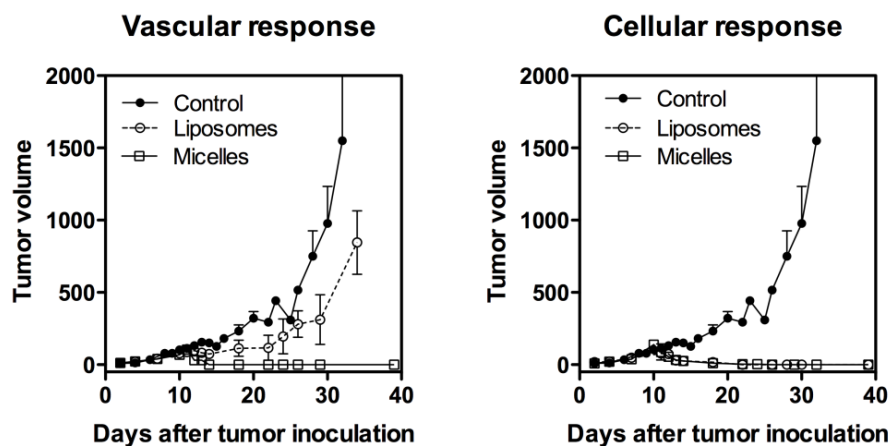
Figure 6.7. Panels A and B) Plots of mean tumor volumes in mice bearing P815 tumor. Points are means of 8-10 tumors and bars are SD. Panels C and D) Kaplan-Meier survival curves of % mice cured from P815 tumors. Vascular response: PDT performed 15 min after i.v. injection of 1 mg/kg formulated temocene. Cellular response: PDT performed 24 h after i.v. injection of 1 mg/kg formulated temocene. Light dose: 150 J/cm^2

Treatments were also tested in a BALB/c mouse tumor model. CT26.CL25 tumor cells were inoculated subcutaneously in the left thigh and the same treatments were performed, namely 1 mg/kg temocene in micellar or liposomal formulation, and 150 J/cm^2 of light dose at 15 min or 24 h after injection. Under these conditions, all treatments worked perfectly resulting in a total tumor regression 4 days after PDT performance (Fig. 6.8).
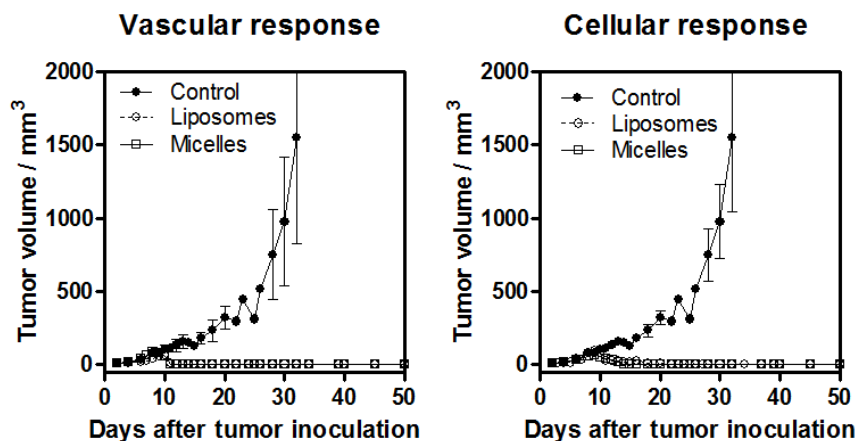
Figure 6.8. Plots of mean tumor volumes in BALB/c mice bearing CT26.CL25 tumor. Points are means of 3-4 tumors and bars are SD. Vascular response: PDT performed 15 min after i.v. injection of 1 mg/kg formulated temocene. Cellular response: PDT performed 24 h after i.v. injection of 1 mg/kg formulated temocene. Light dose: 150 J/cm^2

Only when the light dose was reduced to 75 J/cm^2 (Fig. 6.9) we obtained a differential response. Liposomes in a short drug-to-light interval were not effective and the tumor volume evolution was similar to control group.

Figure 6.9. Plots of mean tumor volumes in BALB/c mice bearing CT26.CL25 tumor. Points are means of 3-4 tumors and bars are SD. Vascular response: PDT performed 15 min after i.v. injection of 1 mg/kg formulated temocene. Cellular response: PDT performed 24 h after i.v. injection of 1 mg/kg formulated temocene. Light dose: 75 J/cm^2

Photobleaching studies during PDT with temocene *in vivo*. We studied the photobleaching of temocene *in vivo* 24 h after i.v. injection of PS encapsulated in micelles or liposomes using the Maestro *in vivo* fluorescence camera system. Fig. 6.10 shows the normalized fluorescence. Results showed that drug delivery system did not affect the photostability of temocene *in vivo*.
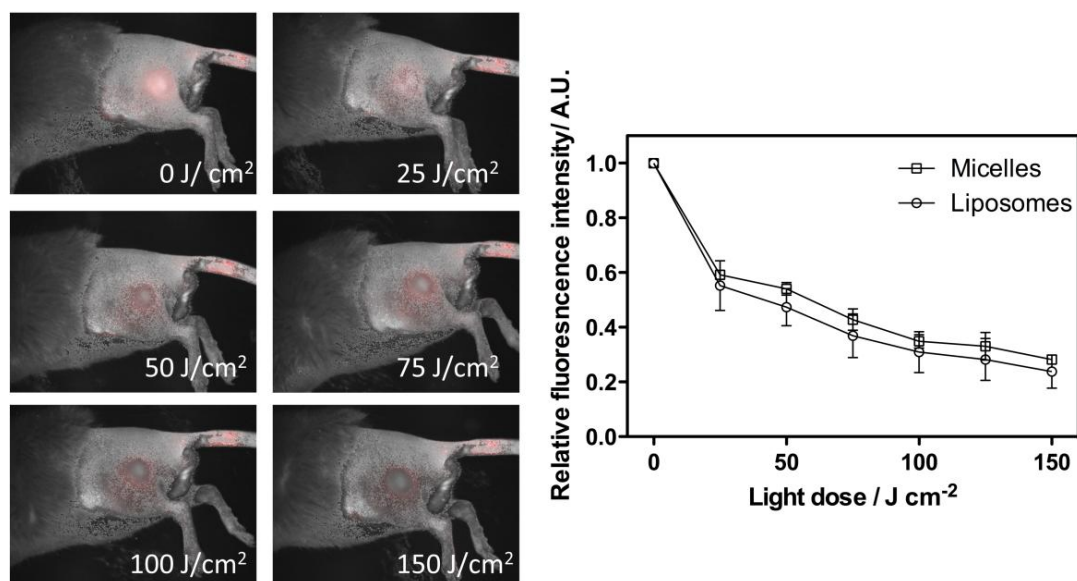
Figure 6.10. *In vivo* photobleaching of temocene encapsulated in micelles or liposomes upon irradiation with 660-nm light source.

Vascular perfusion. Changes of tumor vascular perfusion 1 h after PDT treatment were studied using Hoechst 33342 staining (Fig. 6.11). Compared to control, micellar-vascular treatment led to a significant decrease of tumor vascular perfusion. Hoechst 33342 fluorescence was diffuse along the treated tumor. In contrast, the functional vessels could still be observed after a liposomal-cellular treatment. Mice treated 24 h after PS injection did not show a significant reduction of tumor perfusion area, nor the mice treated 15 min after liposomal temocene injection.
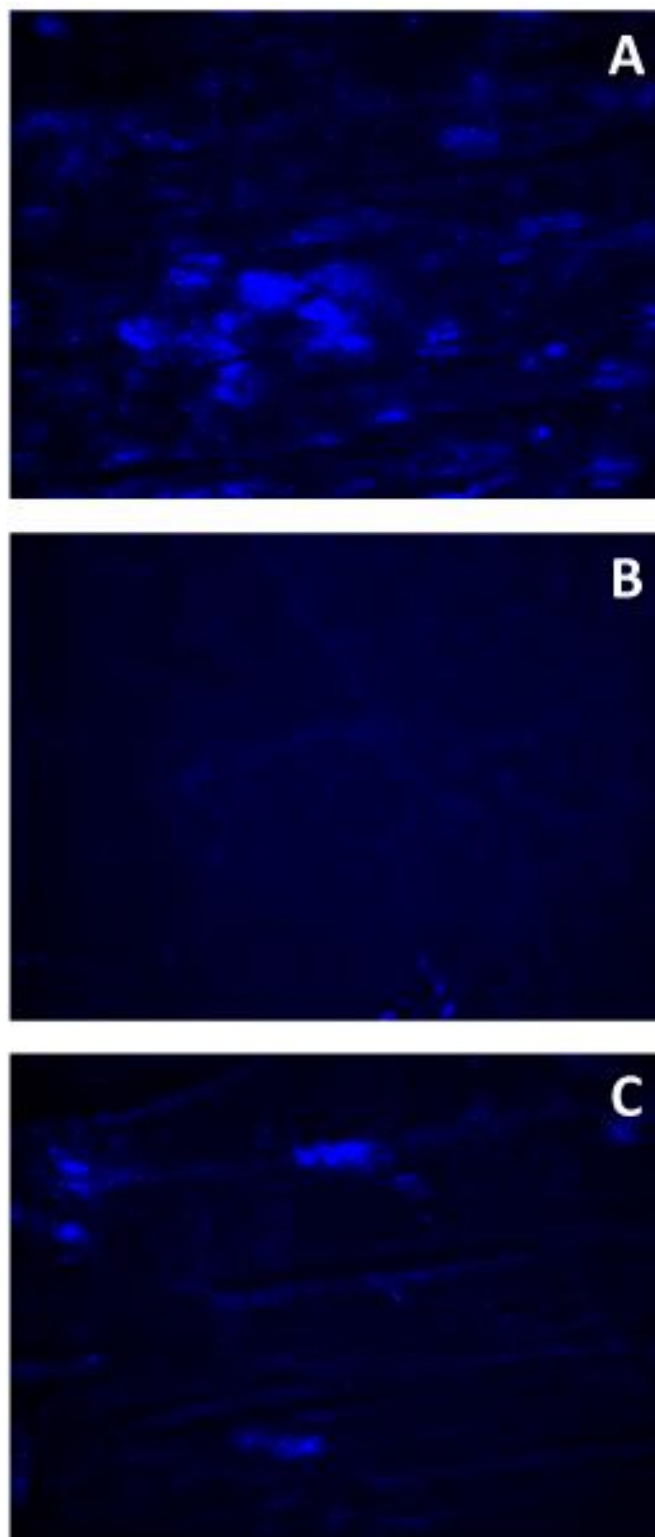
Figure 6.11. Representative fluorescence images of Hoechst 33342-stained images of P815 tumors after PDT (150 J/cm^2) treatment with formulated temocene (1 mg/kg). Panel A) Control tumor. Panel B) 3 h after PDT performed 15 min after micellar injection. Panel C) 3 h after PDT performed 24 h after liposomal injection.

6.4. DISCUSSION

The mechanisms of action for PDT are complex, depending upon the PS, light dosimetry, drug delivery system, and treatment conditions. Temocene (*m*-tetrahydroxyphenyl porphycene) is a novel promising PS whose photophysical properties and *in vitro* PDT efficacy in DMSO were recently studied [19]. However, the inherent unsuitability of DMSO prompted us to consider formulating temocene in different drug delivery systems. The formulation of a PS plays an important role in its activity by modulating the pharmacokinetics, uptake and subcellular distribution and localization. The present study investigated the effect of three different vehicles, namely PEG_{400}/EtOH solutions, Cremophor micelles, and $DPPC/DMPG/PEG_{3000}$-DSPE liposomes, on the PDT effectiveness of temocene.

Micelles, prepared by film formation and hydration just before experiments, and liposomes, prepared by microemulsification and then lyophilized to guarantee a long-term stability during all the experimental stage, allowed for a high encapsulation of temocene in a monomeric state. Aggregation of the PS was evident when delivered in PEG_{400}/EtOH solution. In spite of this fact, this formulation showed the best *in vitro* response because cells were able to internalize the largest amount of PS. However, the killing efficacy per uptaken molecule was higher in the case of liposomes. A minimal internalization and, therefore, no photocytotoxic effect were observed with the micellar formulation. Attempts to modify this situation by adding serum or diluting beyond the critical micellar concentration proved unsuccessful. A literature search revealed that in some circumstances intact micelles are hardly taken up by cells [26-28].

Regarding the subcellular localization of temocene internalized in the different drug delivery systems, *in vitro* experiments performed with organelle-specific fluorescent probes revealed no difference between the vehicles. In all cases, lysosomes were the preferential site of temocene accumulation in P815 cells. These results differed from those obtained in a previous work in HeLa cells although DMSO was used as a vehicle in those studies [19].

Drug delivery systems can also modulate *in vivo* pharmacokinetics and tumor accumulation. P815 tumor bearing mice were studied by non-invasive methods at different times after i.v. injection of the different formulations. Although temocene in PEG/EtOH solution could be considered a promising formulation based on its good *in vitro* response, the formulation failed when it was administered intravenously causing

the immediate death of the mice due to aggregation of the PS in the blood stream. *In vivo* fluorescence imaging studies demonstrated that there was no specific tumor accumulation of temocene after 15 min. On the other hand, the kinetics of tumor uptake with the liposomal formulation showed a higher tumor extravasation reaching its maximum accumulation 24 h after injection. Micelles showed a faster but moderate tumor accumulation. These facts can be explained by the rapid clearance of micelles by reticuloendothelial system and the poor cellular uptake observed *in vitro*. Pegylated liposomes confers steric stabilization and avoids reticuloendothelial system uptake, resulting in prolonged circulation times and enhanced selective localization. The accumulation of macromolecules in tumors is mainly due to the so-called enhanced permeability and retention effect and this progressive phenomenon can be greatly favored by prolonging the half-life in plasma of nanoparticles [17,29,30]. This effect is also dependent of the size of nanoparticles: small carriers can diffuse in and out of the tumor blood vessels because of their small size, and, hence, the effective concentration of the drug in the tumor diminishes compared to larger vehicles [29]. Thus, the difference of size between temocene loaded micelles (30 nm) and liposomes (180 nm) can also affect the extent of drug accumulation in the tumor. Liposomes also showed the best tumor selectivity, namely a tumor-to-normal-tissue ratio of 3.

The time between PS administration and light treatment is also a critical parameter for PDT efficiency. The best PDT response was obtained when light irradiation was delivered 15 min after micelle-loaded temocene injection. This treatment led to a total regression of the tumor with a delay or avoidance of metastasis. This can be rationalized on the basis that P815 tumors express tumor-specific antigens [31-33]. Also, it has been reported that vascular photodynamic therapy can stimulate the immune system by a prompt inflammatory reaction [5,10]. Temocene micelles administered in a vascular regimen thus may promote an immune response that destroys metastatic tumors cells by recognition of tumor-associated antigens. Vascular perfusion results also demonstrate that the major target for the 15-min interval micellar PDT treatment is tumor vasculature causing the disruption of functional blood vessels (Fig. 6.11). However, in contrast to the vascular-targeted bacteriochlorophyll photosensitizers developed by Scherz's group [34,35], the PDT damage of micellar temocene was mainly promoted by the type II mechanism that generates singlet oxygen (Fig. 6.4A), perhaps with a minor contribution of hydroxyl radicals formed *via* a type I mechanism.

In a cellular-targeted regimen, liposomal temocene exhibited the best PDT response. Tumor regrowth was delayed, although not fully prevented, and mouse survival was

improved. In this case, micelles were not effective. These results agree with the 3-fold higher tumor accumulation of the PS attained by liposomes relative to Cremophor micelles.

These results were also corroborated using the BALB/c mouse model tumor. In this case, the higher immunogenicity of CT26.CL25 tumor cells promoted an even better immune response and, hence, a better overall tumor response [36]. Delivery of the same light and drug doses used in the P815 tumor experiments (150 J/cm^2, 1 mg/kg temocene) caused a total regression of tumor in all cases (see supplementary information). Only when the light dose was halved (75 J/cm^2), the vascular response of liposomal formulation had no effect in terms of tumor volume diminution and the advantage of the micellar formulation could be appreciated.

6.5. CONCLUSIONS

We have confirmed that both drug delivery systems and targeting strategy can determine the PDT effectiveness of the new PS temocene both *in vitro* and *in vivo.* Micelles showed no PDT activity in cell cultures, as they were not internalized, while they were the most effective formulation for *in vivo* PDT treatments combined with a short drug-to-light interval. In contrast, temocene in PEG/EtOH solutions could have been regarded as a good vehicle based on the *in vitro* results but caused immediate toxicity when they were administered intravenously. Liposomes are the best vehicle in terms of achieving cell internalization and tumor selectivity.

In conclusion, we have shown that PDT with the novel PS temocene has significant therapeutic effects in a metastatic tumor model, both for a vascular-targeted treatment with its Cremophor EL formulation, and also for a cellular strategy when it is encapsulated in DPPC/DMPG/PEG$_{3000}$-DSPE liposomes.

6.6. REFERENCES

[1] C.A. Robertson, D.H. Evans, H. Abrahamse. Photodynamic therapy (PDT): a short review on cellular mechanisms and cancer research applications for PDT, J. Photochem. Photobiol. B: Biol. 96 (2009) 1-8.

[2] M. Dewaele, T. Verfaillie, W. Martinet, P. Agostinis. Death and survival signals in photodynamic therapy, Methods Mol. Biol. 635 (2010) 7-33.

[3] D.E.J.G. Dolmans, D. Fukumura, R.K. Jain. Photodynamic therapy for cancer, Nat. Rev. Cancer. 3 (2003) 380-387.

[4] B. Krammer. Vascular effects of photodynamic therapy, Anticancer Res. 21 (2001) 4271-4277.

[5] D. Preise, A. Scherz, Y. Salomon. Antitumor immunity promoted by vascular occluding therapy: lessons from vascular-targeted photodynamic therapy (VTP), Photochem. Photobiol. Sci. 10 (2011) 681-688.

[6] B. Chen, B.W. Pogue, J.M. Luna, R.L. Hardman, P.J. Hoopes, T. Hasan. Tumor vascular permeabilization by vascular-targeting photosensitization: effects, mechanism, and therapeutic implications, Clin. Cancer Res. 12 (2006) 917-923.

[7] T.G. St Denis, K. Aziz, A.A. Waheed, Y.Y. Huang, S.K. Sharma, P. Mroz, et al. Combination approaches to potentiate immune response after photodynamic therapy for cancer, Photochem. Photobiol. Sci. 10 (2011) 792-801.

[8] M. Korbelik. Cancer vaccines generated by photodynamic therapy, Photochem. Photobiol. Sci. 10 (2011) 664-669.

[9] P. Mroz, J.T. Hashmi, Y.Y. Huang, N. Lange, M.R. Hamblin. Stimulation of anti-tumor immunity by photodynamic therapy, Expert Rev. Clin. Immunol. 7 (2011) 75-91.

[10] N. Madar-Balakirski, C. Tempel-Brami, V. Kalchenko, O. Brenner, D. Varon, A. Scherz, et al. Permanent occlusion of feeding arteries and draining veins in solid mouse tumors by vascular targeted photodynamic therapy (VTP) with Tookad, PLoS One. 5 (2010) e10282.

[11] S.B. Brown, K.J. Mellish. Verteporfin: a milestone in opthalmology and photodynamic therapy, Expert Opin. Pharmacother. 2 (2001) 351-361.

[12] S. Chevalier, M. Anidjar, E. Scarlata, L. Hamel, A. Scherz, H. Ficheux, et al. Preclinical study of the novel vascular occluding agent, WST11, for photodynamic therapy of the canine prostate, J. Urol. 186 (2011) 302-309.

[13] R.A. Weersink, A. Bogaards, M. Gertner, S.R. Davidson, K. Zhang, G. Netchev, et al. Techniques for delivery and monitoring of TOOKAD (WST09)-mediated photodynamic therapy of the prostate: clinical experience and practicalities, J. Photochem. Photobiol. B: Biol. 79 (2005) 211-222.

[14] C.M. Moore, D. Pendse, M. Emberton. Photodynamic therapy for prostate cancer--a review of current status and future promise, Nat. Clin. Pract. Urol. 6 (2009) 18-30.

[15] D. Bechet, P. Couleaud, C. Frochot, M.L. Viriot, F. Guillemin, M. Barberi-Heyob. Nanoparticles as vehicles for delivery of photodynamic therapy agents, Trends Biotechnol. 26 (2008) 612-621.

[16] W.T. Li. Nanotechology-based strategies to enhance the efficacy of photodynamic therapy for cancers, Curr. Drug Metab. 10 (2009) 851-860.

[17] Y.N. Konan, R. Gurny, E. Allemann. State of the art in the delivery of photosensitizers for photodynamic therapy, J. Photochem. Photobiol. B: Biol. 66 (2002) 89-106.

[18] E. Reddi. Role of delivery vehicles for photosensitizers in the photodynamic therapy of tumours, J. Photochem. Photobiol. B: Biol. 37 (1997) 189-195.

[19] M. García-Díaz, D. Sánchez-García, J. Soriano, M.L. Sagristà, M. Mora, Á Villanueva, et al. Temocene: the porphycene analogue of temoporfin (Foscan®), Med.Chem.Commun. 2 (2011) 616-619.

[20] B. Van den Eynde, B. Lethe, A. Van Pel, E. De Plaen, T. Boon. The gene coding for a major tumor rejection antigen of tumor P815 is

identical to the normal gene of syngeneic DBA/2 mice, J. Exp. Med. 173 (1991) 1373-1384.

[21] M. Wang, V. Bronte, P.W. Chen, L. Gritz, D. Panicali, S.A. Rosenberg, et al. Active immunotherapy of cancer with a nonreplicating recombinant fowlpox virus encoding a model tumor-associated antigen, J. Immunol. 154 (1995) 4685-4692.

[22] F. Postigo, M. Mora, M.A. De Madariaga, S. Nonell, M.L. Sagrista. Incorporation of hydrophobic porphyrins into liposomes: characterization and structural requirements, Int. J. Pharm. 278 (2004) 239-254.

[23] F. Postigo, M.L. Sagrista, M.A. De Madariaga, S. Nonell, M. Mora. Photosensitization of skin fibroblasts and HeLa cells by three chlorin derivatives: Role of chemical structure and delivery vehicle, Biochim. Biophys. Acta. 1758 (2006) 583-596.

[24] H. Hojo, R. Sun, Y. Ono, T. Shishido, E. Obara, Y. Yamazoe, et al. Differential production of interleukin-6 and its close relation to liver metastasis in clones from murine P815 mastocytoma, Cancer Lett. 108 (1996) 55-59.

[25] T. Ohno, M. Inoue, Y. Ogihara. Cytotoxic activity of gallic acid against liver metastasis of mastocytoma cells P-815, Anticancer Res. 21 (2001) 3875-3880.

[26] J.W. Hofman, M.G. Carstens, F. van Zeeland, C. Helwig, F.M. Flesch, W.E. Hennink, et al. Photocytotoxicity of mTHPC (temoporfin) loaded polymeric micelles mediated by lipase catalyzed degradation, Pharm. Res. 25 (2008) 2065-2073.

[27] D. Kessel. Properties of cremophor EL micelles probed by fluorescence, Photochem. Photobiol. 56 (1992) 447-451.

[28] K. Woodburn, C.K. Chang, S. Lee, B. Henderson, D. Kessel. Biodistribution and PDT efficacy of a ketochlorin photosensitizer as a function of the delivery vehicle, Photochem. Photobiol. 60 (1994) 154-159.

[29] A.K. Iyer, G. Khaled, J. Fang, H. Maeda. Exploiting the enhanced permeability and retention effect for tumor targeting, Drug Discov. Today 11 (2006) 812-818.

[30] J. Fang, H. Nakamura, H. Maeda. The EPR effect: Unique features of tumor blood vessels for drug delivery, factors involved, and limitations and augmentation of the effect, Adv. Drug Deliv. Rev. 63 (2011) 136-151.

[31] T.F. Gajewski, M.A. Markiewicz, C. Uyttenhove. The p815 mastocytoma tumor model, Curr.Protoc.Immunol. Chapter 20 (2001) Unit 20.4.

[32] P. Mroz, M.R. Hamblin. Photodynamic therapy stimulates anti-tumor immunity in a murine mastocytoma model, Proc. SPIE. 6857 (2008) 1-9.

[33] B. Lethe, B. van den Eynde, A. van Pel, G. Corradin, T. Boon. Mouse tumor rejection antigens P815A and P815B: two epitopes carried by a single peptide, Eur. J. Immunol. 22 (1992) 2283-2288.

[34] Y. Vakrat-Haglili, L. Weiner, V. Brumfeld, A. Brandis, Y. Salomon, B. McLlroy, et al. The microenvironment effect on the generation of reactive oxygen species by Pd-bacteriopheophorbide, J. Am. Chem. Soc. 127 (2005) 6487-6497.

[35] I. Ashur, R. Goldschmidt, I. Pinkas, Y. Salomon, G. Szewczyk, T. Sarna, et al. Photocatalytic generation of oxygen radicals by the water-soluble bacteriochlorophyll derivative WST11, noncovalently bound to serum albumin, J. Phys. Chem. A. 113 (2009) 8027-8037.

[36] P. Mroz, A. Szokalska, M.X. Wu, M.R. Hamblin. Photodynamic therapy of tumors can lead to development of systemic antigen-specific immune response, PLoS One. 5 (2010) e15194.

Chapter 7

New models for predicting *in vitro* the PDT outcome

Singlet oxygen photosensitization in 3D cultures and *ex-vivo* skin samples

Singlet oxygen ($^1O_2$) is believed to be the major cytotoxic agent involved in photodynamic therapy (PDT) both *in vitro* and *in vivo* but accurate quantification is technically challenging, especially in biological systems. Three-dimensional (3D) culture models represent a powerful bridge between conventional cell monolayers and complex biological tissues, whereas *ex-vivo* skin samples are useful for predicting the outcome of dermatological photo-oxidation processes. Here we report for the first time on the kinetics of $^1O_2$ formation and PDT response in an *in vitro* 3D model based on culturing human fibroblasts in the self-assembling hydrogel RAD16-I. Finally, we have studied the effect of Lipochroman-6, a quencher used in cosmetic and pharmaceutical formulations on singlet oxygen kinetics of by means of *ex-vivo* skin samples. Taken together, these new *in vitro* models offer a new approach to study $^1O_2$ mobility in complex systems and a powerful tool that better mimic the PDT and other photo-oxidation responses.

7.1. INTRODUCTION

Singlet oxygen ($^1O_2$) is believed to play a major role in many photo-oxidation processes, such as skin aging, inflammation, or radiation damage; and in light-mediated treatments, particularly in photodynamic therapy (PDT). For these reasons, major efforts have been made to develop assays for measuring $^1O_2$ generated within cultured cells and intact living organisms [1-9]. Time-resolved measurement of $^1O_2$ phosphorescence centered at 1275 nm is now a very well-established method for monitoring $^1O_2$ [10-12]. The kinetics of $^1O_2$ emission provides information about the photosensitizer (PS) triplet excited state and $^1O_2$ lifetimes within the cell, offering a powerful tool for studying the oxygen-cell interactions. The ability to detect $^1O_2$ luminescence in biological environments has been attempted previously [3,6,7,9] and the mobility of $^1O_2$ within cells and tissues has been subject of debate for the last two decades [13-16]. Several investigators have reported results from cell suspensions [3,9], single cells [1,13], and even in living tissues [6,17]. However, the *in vivo* detection of $^1O_2$ remains technically difficult and the results are still ambiguous.

To better understand the behavior of $^1O_2$ in complex systems, we have monitored the kinetics of $^1O_2$ and the photosensitizer's phosphorescence in a three-dimensional (3D) culture model, carrying out parallel experiments on a classical two-dimensional (2D) culture model as controls.

3D cell cultures were selected as study model because it is well reported that they reproduce the hierarchical complexity of human tissues and organs more precisely than conventional monolayer cultures, providing a potential bridge for the gap between 2D cell cultures and animal models [18-20]. Specifically, 3D models can better integrate the chemical, physical and mechanical signals that cells receive from the extracellular matrix (ECM) and their neighboring cells [18]. For instance, the ECM affects both solute binding and diffusion, generating local gradients of oxygen, nutrients, metabolites and signaling molecules that are continuously consumed and produced by cells [21-23]. Instead, 2D cultures are characterized by uniformly rich nutrition and oxygenation [24], affecting their response to oxygen-dependent processes.

In the present work, we developed an *in vitro* 3D model based on culturing human fibroblasts in the self-assembling hydrogel RAD16-I. This scaffold forms a network of interweaving nanofibers of 10-20 nm diameter and 50-200 nm pore size, surrounding cells in a similar manner to the natural extracellular matrix and, thereby, mimicking the

in vivo cellular environment [25-29]. RAD16-I hydrogel has previously been shown to promote growth and proliferation of multiple cell types, including fibroblasts, chondrocytes, hepatocytes, endothelial cells, osteoblasts and neuronal cells, as well as embryonic and somatic stem cells [30-37]. We demonstrated that cells in this 3D culture model are exposed to non-uniform distribution of oxygen and nutrients, which produces a heterogeneous population of cells that differ in their response to oxygen-dependent therapies, such as photodynamic therapy.

A further increase in the level of biological complexity is provided by *ex-vivo* skin samples, which are often used as models for predicting the outcome of wound healing, skin penetration and other dermatological treatments, including PDT [38-42]. In this work we used *ex-vivo* porcine skin samples for studying the $^1O_2$ quenching ability of the antioxidant Lipochroman-6 (LC-6) (Fig. 7.1) in skin. Due to its interface function between the body and environment, skin is chronically exposed to both endogenous and environmental pro-oxidant agents. Endogenous PS such as flavins, porphyrins or NADH/NAD [43-46] as well as exogenous molecules administered to skin along with cosmetic or medical treatments [47,48] are a source of light-driven $^1O_2$ formation under UVA exposure. Based on this rationale, the inclusion of antioxidants in cosmetic preparations is an increasing trend [49,50]. LC-6 is a powerful antioxidant used in cosmetic and pharmaceutical formulations. It has been demonstrated that LC-6 prevents lipid peroxidation and is an efficient reactive oxygen and nitrogen species scavenger [51-55]. Since the structure of LC-6 resembles that of □-tocopherol (Fig. 7.1), a common antioxidant that has been described as an effective singlet oxygen quencher [56], it seems plausible that LC-6 antioxidant activity is at least partially due to quenching of singlet oxygen. But traditional measurements in solution or cell cultures may not reproduce the complexity of skin. In this work we demonstrated that the antioxidant effect of LC-6 in skin differed from that obtained in solution.

A Lipochroman-6
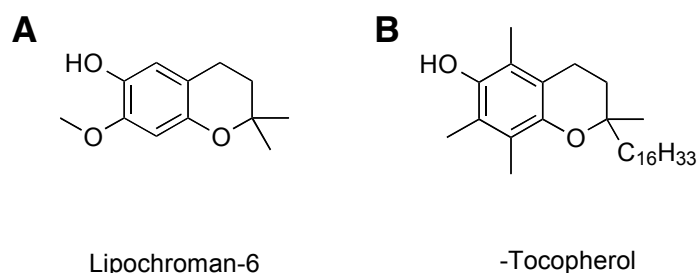
B -Tocopherol

Figure 7.1. Chemical structures of (A) LC-6 and (B) α-tocopherol.

7.2. EXPERIMENTAL SECTION

Chemicals. LC-6 and α-tocopherol were supplied by Lipotec S.A. and were certified to be of purity higher than 96%. Creams and porcine skin were also supplied by Lipotec S.A. 5,10,15,20-tetrakis(*N*-methyl-4-pyridil)-21*H*,23*H*-porphine (TMPyP, 97%), 1*H*-phenalen-1-one (PN, 97%) and 5,10,15,20-Tetraphenyl-21*H*,23*H*-porphine (TPP, ≥ 99%) were purchased from Sigma-Aldrich Chemical Co. (St. Louis, MO). Deuterium oxide (99.9%) and methanol-d_4 (99.8%) were purchased from Solvents Documentation Synthesis (SDS, Peypin, France). All other chemicals were commercially available reagents of at least analytical grade.

3D culture technique. 3D cell cultures were performed by Mireia Alemany-Ribes as part of her Ph.D. thesis and are included in this chapter to facilitate the understanding of how 3D cell constructs are cultured.

Very briefly, self-assembling peptide scaffolds were prepared by diluting 1% (w/v) RAD16-I (PuraMatrix™, BD Biosciences, Frankin Lakes, NJ) in 25% (w/v) sucrose in order to obtain a final concentration of 0.6% (w/v) RAD16-I. The peptide solution was sonicated for 5 min. Human normal dermal fibroblasts (hNDF) were harvested by tripsinization from the 2D culture flask and suspended in 10% (w/v) sucrose to get a final concentration of $4 \cdot 10^6$ cells/mL. Then, equal volumes of cell suspension and 0.6% RAD16-I were mixed to obtain a final suspension. 40 μL of this suspension were loaded into 30 mm diameter cell culture inserts (Millipore, Billerica, MA), previously placed inside 6-well culture plates and wet with supplemented DMEM. The medium penetrated the insert from the bottom membrane, inducing the self-assembling process. Finally, a total volume of 2 mL of encapsulation medium was added into the insert in consecutive small portions, favoring the leaching of the sucrose. The remaining medium in the well, rich in sucrose was replaced with fresh medium, which was change every day by removing 500 μL from the well and adding 500 μL of fresh medium into the insert.

Spectroscopic measurements in cell suspensions, 3D cultures and RAD16-I peptide scaffold. An appropriate number of cells were seeded in 75 cm^2 flasks and were cultured to 80% confluence. They were incubated in the dark with 100 μM TMPyP for 24 hours. The medium was discarded and the cells were washed three times with PBS, trypsinized and resuspended in 1.5 mL of PBS or d-PBS to a final concentration of 4 million cells/mL. The cell suspensions were continuously stirred during the measurements.

For measurements in 3D cultures, cell constructs were prepared as described above. They were incubated in the dark with 100 μM TMPyP for 24 hours, washed 3 times with PBS and carefully transferred to a 1-cm quartz cuvette. For D$_2$O-based measurements, cell constructs were incubated with d-PBS for 20 min before measurements to exchange the extracellular H$_2$O with D$_2$O.

For control measurements in RAD16-I peptide scaffold without cells peptide gel formation through a self-assembling process was performed directly in a 0.4-cm quartz cuvette wall. When hydrogel was formed, peptide scaffold was incubated in the dark with 100 μM TMPyP for 24 hours. The cuvette was washed several times with PBS or d-PBS until no signal measured in supernatant fluid.

For time-resolved phosphorescence measurements, cell suspensions, 3D culture cell constructs or RAD16-I peptide scaffolds were irradiated with 10 million laser pulses at 532 nm. Appropriated controls were performed to ensure that the signals originated from the photosensitizer molecules internalized. Spectroscopic measurements were carried out within the following 45 min.

LC-6 quenching of singlet oxygen in porcine skin. 15 mg (5 mg/cm^2) of LC-6 formulations containing 3% of PN or TPP were spread on porcine skin samples over the whole surface using a glove-coated finger. Measurements were carried out 15 min later to allow for cream penetration in the skin. Five measurements were recorded at different positions of the skin and averaged to compensate for sample inhomogeneities. A placebo cream (without LC-6) and a α-tocopherol containing cream were used as negative and positive controls, respectively.

7.3. RESULTS AND DISCUSSION

7.3.1. Singlet oxygen photosensitization in 3D cultures

Measurement of intracellular TMPyP fluorescence. The photophysical properties of TMPyP show a remarkable dependence with the microenviroment in which the photosensitizer is located. Fig. 7.2 shows the steady state and time-resolved emission spectra of TMPyP incorporated in cell suspension, 3D cultures and peptide scaffold. The fluorescence emission spectra of intracellular TMPyP, both 2D and 3D, showed two well-resolved bands, in contrast to the structure-less broad band in peptide scaffold. Time-resolved measurements provide an additional evidence of the photosensitizer localization. In RAD16-I, the fluorescence observed at 650 nm, decayed monoexponentially with a lifetime of 5.1 ± 0.3 ns. In contrast, signals obtained from TMPyP incorporated to cells required three exponentials terms. For cell suspensions, a triexponential decay can be fitted with lifetimes of 0.8 ± 0.1, 3.5 ± 0.3 and 11 ± 0.5 ns. The fluorescence of TMPyP incorporated in 3D cultures decays with lifetimes of 1.3 ± 0.1, 4.9 ± 0.3 and 11 ± 0.5 ns.
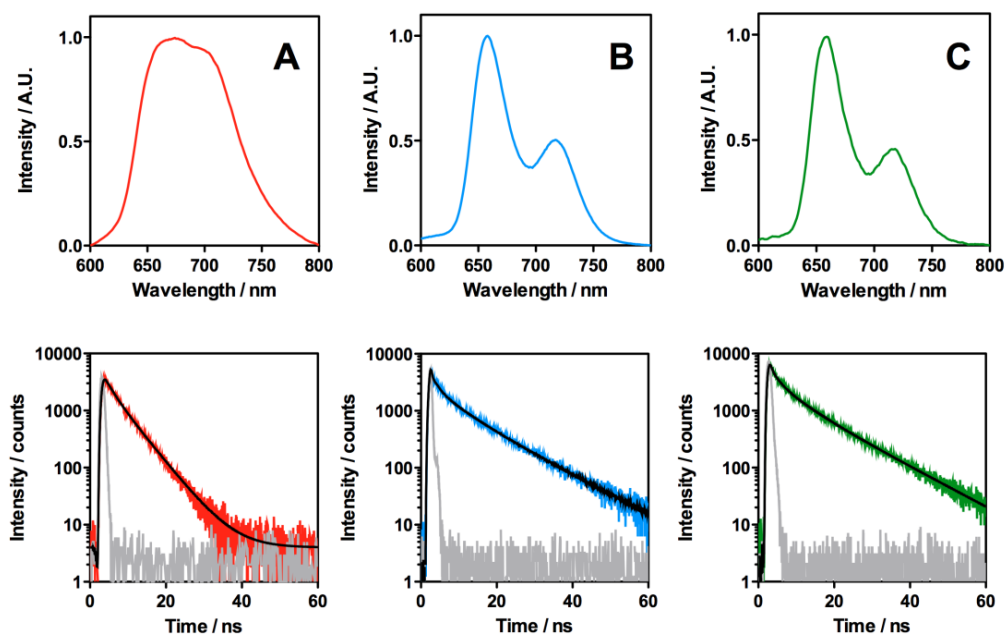

Figure 7.2. Normalized steady state and time-resolved fluorescence emission spectra of TMPyP previously incorporated in (A) RAD16-I scaffold without cells; (B) hNDF suspension; and (C) hNDF 3D cultures.

Detection of singlet oxygen luminescence in cell suspensions, 3D cultures and RAD16-I peptide. The $^1O_2$ luminescence at 1275 nm and TMPyP phosphorescence at 960 nm signals from hNDF in 3D cultures are shown in Fig. 7.3. The $^1O_2$ signal observed at 1275 nm grew with a lifetime of $^{1275}\tau_1^{3D,PBS}$=2.1 ± 0.5 μs and decayed biexponentially with lifetimes of $^{1275}\tau_2^{3D,PBS}$=7 ± 2 μs and $^{1275}\tau_3^{PBS}$=32 ± 2 μs, respectively. At 960 nm, the phosphorescence signal decayed with two exponential terms, $^{960}\tau_1^{3D,PBS}$=5 ± 2 μs and $^{960}\tau_2^{3D,PBS}$=29 ± 2 μs, respectively. It is well known that the lifetime of $^1O_2$ is increased in deuterated solvents [57]. Irradiation of hNDF cells in 3D cultures produce a significantly change in the phosphorescence signals. At 1275 nm, the signals grew with a lifetime of $^{1275}\tau_1^{3D,dPBS}$=7 ± 2 μs, and decayed biexponentially with lifetimes of $^{1275}\tau_2^{3D,dPBS}$=27 ± 5 μs and $^{1275}\tau_3^{dPBS}$=56 ± 5 μs, respectively. At 960 nm, the phosphorescence signal showed the same kinetics as in PBS, namely $^{960}\tau_1^{dPBS}$=7 ± 2 μs and $^{960}\tau_2^{dPBS}$=32 ± 2 μs, respectively. The addition of 0.75 mM BSA, an efficient $^1O_2$ quencher that cannot penetrate the cells [58], to d-PBS suspensions only induced a significant change to the large component on the $^1O_2$ decay signal, yielding a $^{1275}\tau_1^{3D,BSA}$=6 ± 2 μs for the raise and $^{1275}\tau_2^{3D,BSA}$=27 ± 2 μs and $^{1275}\tau_3^{3D,BSA}$=40 ± 2 μs for the decay. However, the addition of 35 mM NaN$_3$, a well-known $^1O_2$ quencher that readily enters the cells from the extracellular medium [6,13], the typical rise and decay signal of $^1O_2$ phosphorescence disappears, leading to a monoexponential decay $^{1275}\tau_1^{azide}$=5 ± 2 μs. The same kinetics is observed at 960 nm, namely $^{960}\tau_1^{azide}$=4.3 ± 0.5 μs.

As parallel controls, the same measurements were carried out in cell suspensions and RAD16-I peptide scaffold. The $^1O_2$ luminescence at 1275 nm and TMPyP phosphorescence at 960 nm signals from hNDF cell suspensions are shown in Fig. 7.3. For cells suspended in PBS, the $^1O_2$ signal observed at 1275 nm showed, as in case of 3D cultures, a triexponential behavior, although in this case grew with a lifetime of $^{1275}\tau_1^{2D,PBS}$=3.2 ± 0.2 μs and decayed with lifetimes of $^{1275}\tau_2^{2D,PBS}$=4.3 ± 0.2 μs and $^{1275}\tau_3^{2D,PBS}$=32 ± 2 μs, respectively. At 960 nm, the phosphorescence signal decayed with two exponential terms, $^{960}\tau_1^{2D,PBS}$=3.3 ± 0.5 μs and $^{960}\tau_2^{2D,PBS}$=28 ± 2 μs, respectively. Irradiation of hNDF cells in d-PBS suspension produce again a significantly change in the phosphorescence signals. At 1275 nm, the signals grew with a lifetime of $^{1275}\tau_1^{2D,dPBS}$=3.1 ± 0.5 μs, and decayed biexponentially with lifetimes of $^{1275}\tau_2^{2D,dPBS}$=33 ± 2 μs and $^{1275}\tau_3^{2D,dPBS}$=59 ± 5 μs, respectively. At 960 nm, the phosphorescence signal showed the same kinetics as in PBS, namely $^{960}\tau_1^{2D,dPBS}$=4.3 ± 0.5 μs and $^{960}\tau_2^{2D,dPBS}$=32 ± 2 μs, respectively. Only the long component of the $^1O_2$

decay is affected by the addition of 0.75 mM BSA to dPBS cell suspensions. However, the addition of 35 mM NaN_3 caused the disappearance of the typical rise and decay signal of $^1O_2$ phosphorescence. The same kinetics was observed at 960 nm.
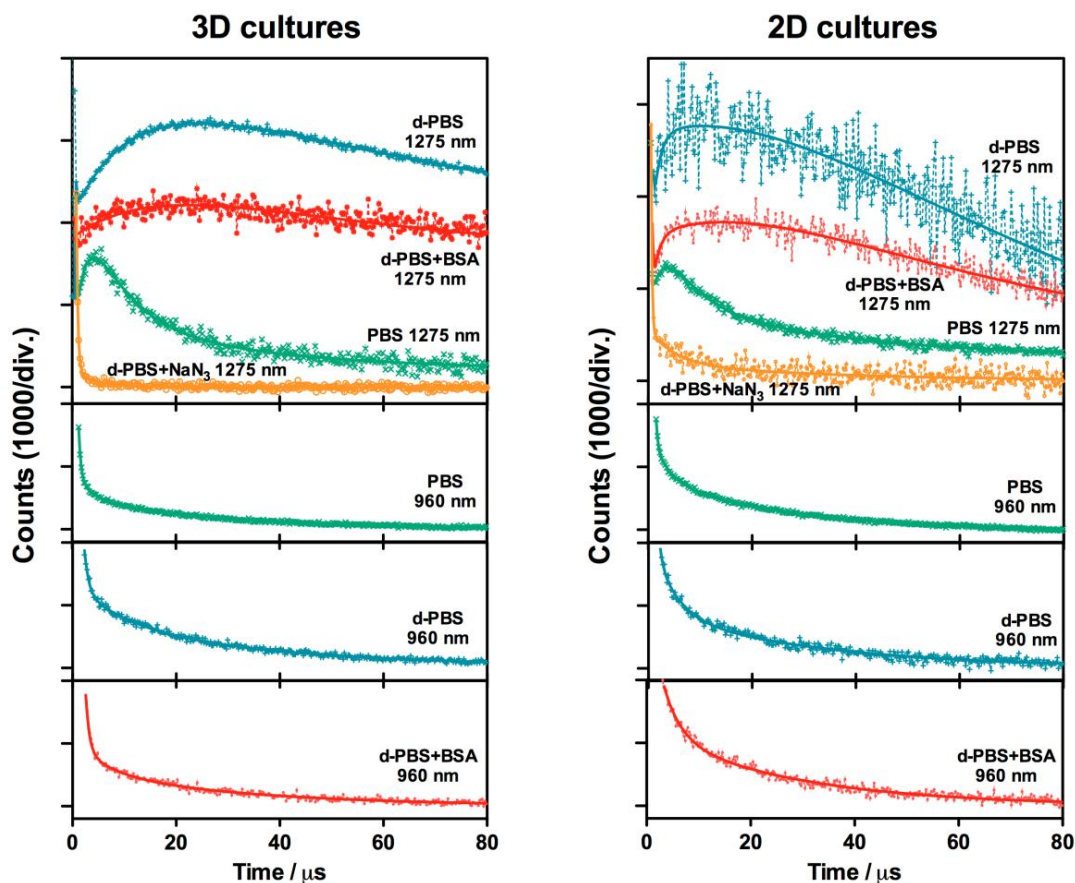
Figure 7.3. 3D and 2D cultures: Singlet oxygen phosphorescence at 1275 nm and TMPyP phosphorescence at 960 nm. The curves are shifted up for illustration.

$^1O_2$ luminescence at 1275 nm and TMPyP phosphorescence at 960 nm signals from RAD-16I peptide scaffold are shown in Fig. 7.4 The $^1O_2$ signal observed at 1275 nm in PBS can be fitted with two exponentials, yielding $^{1275}\tau_1^{peptide,PBS}=1.6 \pm 0.2$ μs and $^{1275}\tau_2^{peptide,PBS}=3.5 \pm 0.2$ μs. The decay of the phosphorescence at 960 nm can be fitted with a single exponential $^{960}\tau_1^{peptide,PBS}=1 \pm 0.5$ μs. The isotope effects were evidenced

when PBS was replaced with D_2O. The signal disappeared when 0.75 mM BSA or 35 mM NaN_3 were added to the peptide containing cuvette.
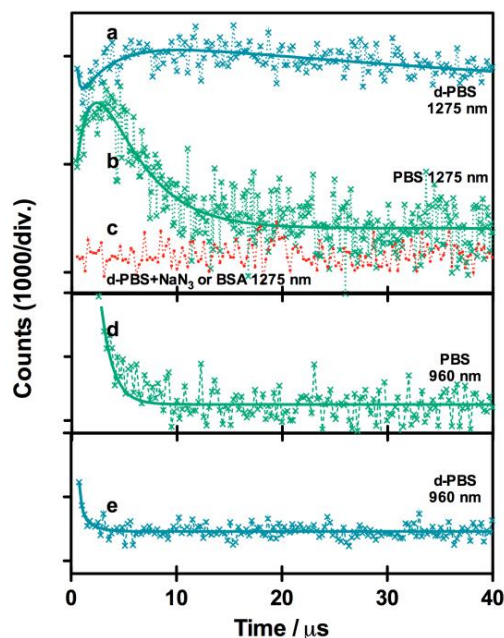

Figure 7.4. RAD16-I scaffold: Singlet oxygen phosphorescence at 1275 nm and TMPyP phosphorescence at 960 nm. The curves are shifted up for illustration.

Discussion. PDT efficacy *in vivo* depends on a number of parameters including tissue oxygenation, photosensitizer concentration and distribution and light dosimetry. However, most of these factors are poorly reproduced by conventional *in vitro* studies that fail to account for extracellular barriers that are present *in vivo* and the differences in cell phenotype between cells cultured as monolayers and cells in native tissue. 3D culture systems are regarded as a bridge between these two systems that better mimic *in vivo* conditions. In order to better understand the photosensitizer distribution and singlet oxygen production inside the tissue we compared the kinetics of both singlet oxygen and photosensitizer phosphorescence in cellular suspensions and 3D cell cultures.

The subcellular localization of a photosensitizer is usually assessed by fluorescence microscopy techniques and this has been done in the 3D cultures as well (see below). The photophysical approach showed that TMPyP was internalized by cells in 3D cultures and it was hardly retained by the peptide nanofibers. When TMPyP was

incubated in RAD16-I scaffold without cells, the kinetics and the structure-less profile of fluorescence emission indicated that TMPyP was located in an aqueous-like environment. However, the incubation in 3D cultures led to a well-resolved fluorescence emission spectrum with two peaks, indicating a change in the TMPyP microenvironment. The fluorescence spectra of TMPyP incorporated in cell suspensions showed similar structure to that obtained in 3D cell cultures. Thus, it can safely be concluded that the photosensitizer in 3D cultures is located within the cells and is not retained by the scaffold. This conclusion is reasserted by time-resolved fluorescence measurements. The lifetime of the fluorescence in RAD16-I scaffold (5.1 ns) revealed an aqueous-like environment located in the buffer pools of the peptide network. The fact that the lifetime was slightly longer than the typical value in buffered solution (4.6 ns, [59]) would indicate that the TMPyP was partially attracted by the negative charges of the peptide sequence of the scaffold, restraining the rotation and vibration of the molecules. Whereas in RAD16-I scaffold the fluorescence kinetics were monoexponential, the fluorescence of TMPyP in the cells presented a multiexponential decay. The lifetimes of 1.5, 5.7 and 12 ns suggest two subcellular localizations of the photosensitizer. It has been shown that upon irradiation of TMPyP in a cell, the photosensitizer can relocalize into a different subcellular domain [60,61]. The initial lysosomal localization rapidly changes to the cell nucleus upon irradiation. TMPyP bound to DNA led to double-exponential decays with lifetimes of 2 and 11 ns [59,62], whereas the lifetime of 5.7 ns can be attributed to the remaining lysosomal distribution. That holds true for both 2D and 3D cultures. It is important to emphasize that the 3D culture model does not affect the intracellular localization of the photosensitizer, which is evidenced with the similar fluorescence emission kinetics of both cellular suspensions and 3D cultures.

The dual localization of TMPyP was corroborated by confocal microscopy. TMPyP was clearly localized in the cytoplasmic vacuoles (lysosomes among others) and after irradiation the photosensitizer appeared bound to DNA in the nucleus (Fig. 7.5).
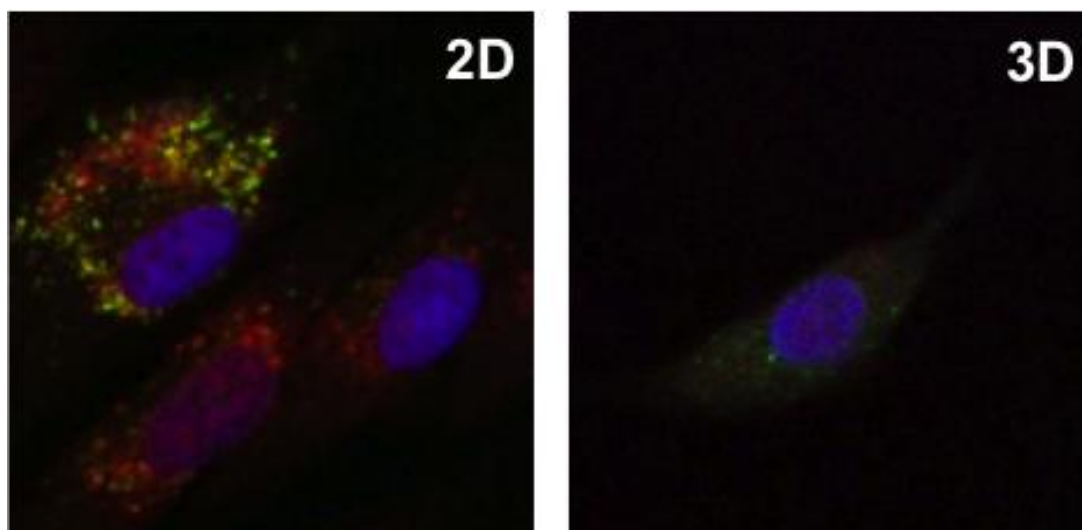
Figure 7.5. Fluorescence microscopy images of hNDF in 2D and 3D cell cultures showing red fluorescence from TMPyP overlaid with green fluorescence of lysotracker and blue fluorescence of DAPI (nucleus). Confocal experiments performed by Mireia Alemany-Ribes.

The observed kinetics of ^{3}PS and $^1O_2$ can be interpreted in light of these findings. First of all, the dual localization of TMPyP is reflected in his triplet-state kinetics, as evidenced by the biexponential decay of its phosphorescence at 960 nm in both 3D and cell suspensions. Thus, we can assign the longer component to molecules localized in the nucleus, consistently with previous works that reported that molecules bound to DNA become less susceptible to the quenching effect of oxygen [1,63]. The short component of the ^{3}TMPyP phosphorescence can be assigned to the remaining PS in the lysosomes. This triplet lifetime had a longer life in 3D cultures (7 ± 2 µs *vs.* 4 ± 0.5 µs in cell suspensions), which indicates less accessibility or oxygen concentration in 3D cultures. This reflects the heterogeneous distribution of oxygen in this type of cultures and it is consistent with the differential PDT effects and the upregulation of hypoxia genes expression (see Mireia Alemany-Ribes Ph.D. thesis for details).

Likewise, the kinetics of $^1O_2$ phosphorescence at 1275 nm reflects the $^1O_2$ localization and mobility. A summary of the lifetimes recorded is given in Table 7.1.

Table 7.1. $^1O_2$ kinetic parameters in air-equilibrated aqueous suspensions of different systems incubated with TMPyP[a].

| System	Solvent	τ_{T1}, μs	τ_{T2}, μs	τ_{Δ}, μs
RAD16-I	H_2O	1.6 ± 0.2	-	3.5 ± 0.2
	D_2O	2 ± 0.2	-	67 ± 2
	D_2O / 0.75 mM BSA	-	-	-
2D suspensions	H_2O	4.3 ± 0.5	32 ± 2	3.2 ± 0.2
	D_2O	3.1 ± 0.5	33 ± 2	67 ± 2
	D_2O / 0.75 mM BSA	3 ± 0.5	28 ± 4	47 ± 2
	D_2O / 35 mM NaN_3	4 ± 1	34 ± 5	-
3D cultures	H_2O	7 ± 2	32 ± 2	3.1 ± 0.5
	D_2O	7 ± 2	28 ± 2	56 ± 5
	D_2O / 0.75 mM BSA	5 ± 2	27 ± 2	40 ± 5
	D_2O / 35 mM NaN_3	5 ± 2	-	-

[a] Mean ± SD values of at least three experiments are shown.

In agreement with [64] $^1O_2$ decays with a single lifetime, irrespective of the site of formation, suggesting a fast equilibration between the different populations before its decay. For RAD16-I system, τ_{Δ} values are similar to those obtained in aqueous solution (3.5 μs in PBS and 67 μs in D-PBS), reaffirming the hypothesis that the photosensitizer localizes in the water pools of the peptide matrix. For cell suspensions, we can identify τ_{Δ} = 3.2 ± 0.2 μs for H_2O-based measurements and τ_{Δ} = 67 ± 2 μs when they were carried out in D_2O-PBS. A slight decrease of $^1O_2$ lifetimes was observed in 3D systems. A lifetime of τ_{Δ} = 3.1 ± 0.2 μs can be fitted for H_2O-based experiments, whereas τ_{Δ} = 56 ± 5 μs in D_2O-mediated measurements. These data indicate a moderate amount of singlet oxygen quenching by the proteins of the ECM or a hampered mobility. A small fraction of $^1O_2$ molecules was able to diffuse out of the cells. On the addition of 0.75 mM of BSA to the extracellular medium, $^1O_2$ lifetime was slightly quenched yielding τ_{Δ} = 47 ± 2 μs for cells suspensions and τ_{Δ} = 40 ± 5 μs for 3D systems. This is consistent with other works that reported the mobility of singlet oxygen inside the cells [3,14]. Due to the restriction of $^1O_2$ diffusion coefficient in the 0.4-2 x 10^{-5} cm^2 s^{-1}, singlet oxygen can diffuse a short distance relative to cellular dimensions, independently of the extracellular media (suspension or a cluster of cells). Therefore, we can only see slight changes in the $^1O_2$ phosphorescence kinetics.

There are at least two populations of TMPyP molecules inside de cells (both in 2D and in 3D cultures), with different localizations and different triplet excited state lifetimes. Moreover, the longer triplet lifetime when TMPyP is incubated in a three-dimensional

system evidenced a lower oxygen concentration, which is corroborated with the overexpression of hypoxia genes inside the 3D construct.

7.3.2. Singlet oxygen photosensitization in skin

LC-6 quenching of singlet oxygen in solution. The time-resolved $^1O_2$ phosphorescence curves for each LC-6 solution are collected in Fig. 7.6A. In the absence of LC-6, the lifetime of $^1O_2$ was 210 ± 20 μs, which agrees well with the published value of 240 ± 20 μs in CD_3OD [65]. Addition of LC-6 resulted in a clear decrease of the $^1O_2$ lifetime τ_Δ. From the plot of the decay rate constant k_Δ (=$1/\tau_\Delta$) as a function of LC-6 concentration, the value of the quenching rate constant k_{LC6} = (1.3 ± 0.1) x 10^8 M^{-1} s^{-1} was determined (Fig. 7.6B).
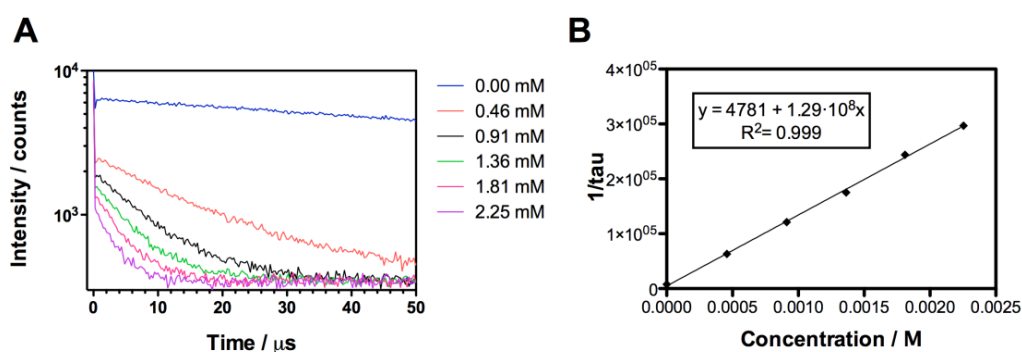
Figure 7.6. Effect of LC-6 on the kinetics of singlet oxygen decay in methanol-d_4. A) Time-resolved singlet oxygen phosphorescence curves recorded at 1275 nm upon irradiation of PN solution containing different concentrations of LC-6. B) Stern-Volmer plot of PN solution upon addition of increasing amounts of LC-6.

LC-6 quenching of singlet oxygen in skin. A similar approach was followed to probe the effect of LC-6 on singlet oxygen in ex-vivo samples of porcine skin. Because skin is a heterogeneous medium, five time-resolved $^1O_2$ phosphorescence curves, recorded at different positions of skin, were averaged for each formulation tested. In a first series of experiments, formulations containing PN as photosensitizer were applied to the skin and, after 15 min of penetration, $^1O_2$ phosphorescence measurements were carried out. Fig. 7.7 shows the 1275-nm time-resolved luminescence signals for the different formulations in skin. When placebo was applied to porcine skin, the decay time of

singlet oxygen luminescence grew with a lifetime of τ_1 = 0.8 ± 0.3 μs and decayed with a lifetime of τ_2 = 18 ± 2 μs (Fig. 7.7A). The shortest of the two was assigned to the formation of $^1O_2$ and thus to the decay of the triplet PN precursor (τ_T), while the longest was assigned to $^1O_2$ decay (τ_Δ). Baier et al. reported a $^1O_2$ lifetime of 8 ± 2 μs in a similar *ex-vivo* porcine skin model [4]. The presence of LC-6 in the formulations induced significant changes to the $^1O_2$ kinetics (Figs. 7.7B and C). At LC-6 0.05% w/w, the lifetime of singlet oxygen dropped to $\tau_{\Delta 1}$ = 5 ± 2 μs and an additional long-lived decay component could be observed with $\tau_{\Delta 2}$ = 13 ± 2 μs (relative amplitude 1:2). For comparison, α-tocopherol at 0.1 % w/w quenched both the formation and the decay of singlet oxygen, yielding a low intensity signal with lifetime τ_Δ = 3 ± 2 μs (Fig. 7.7D).
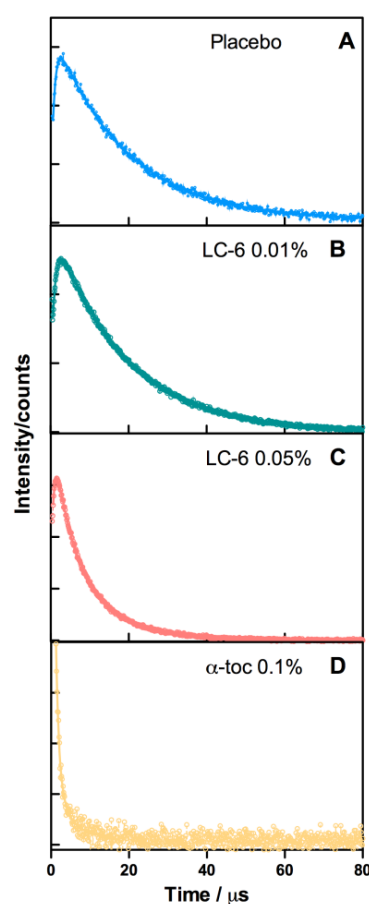
Figure 7.7. Time-resolved luminescence decays recorded on 355 nm excitation of ex-vivo porcine skin treated with different PN containing formulations. A) Placebo cream. Fitted parameters: τ_T= 0.8 ± 0.3 μs; τ_D= 18 ± 2 μs. B) LC-6 0.01% cream. Fitted parameters: τ_T= 0.9 ± 0.3 μs; τ_D= 18 ± 2 μs. C) LC-6 0.05% cream. Fitted parameters: τ_T= 0.8 ± 0.2 μs; τ_{D1}= 5 ± 2 μs; τ_{D2}= 13 ± 2 μs. D) α-tocopherol cream. Fitted parameter: τ_D= 3 ± 2 μs.

PN, as a partially water soluble molecule, can localize in both the lipid and aqueous compartments of the skin. However, the high lipophilicity of LC-6 suggests its preferential accumulation in hydrophobic domains. In order to ensure a closer proximity between the nascent $^1O_2$ and LC-6, a more hydrophobic photosensitizer was used in another series of experiments. TPP was used to this end [65]. As with PN, the NIR emission spectra showed a maximum at 1275 nm, which is the unambiguous spectroscopic fingerprint of singlet oxygen (Fig. 7.8). Consistent with the lifetime decrease observed with PN, the $^1O_2$ phosphorescence dropped by ca. 50% when LC-6 0.05% was added to the cream. Under the same conditions, α-tocopherol led to almost complete depletion of the $^1O_2$ emission.
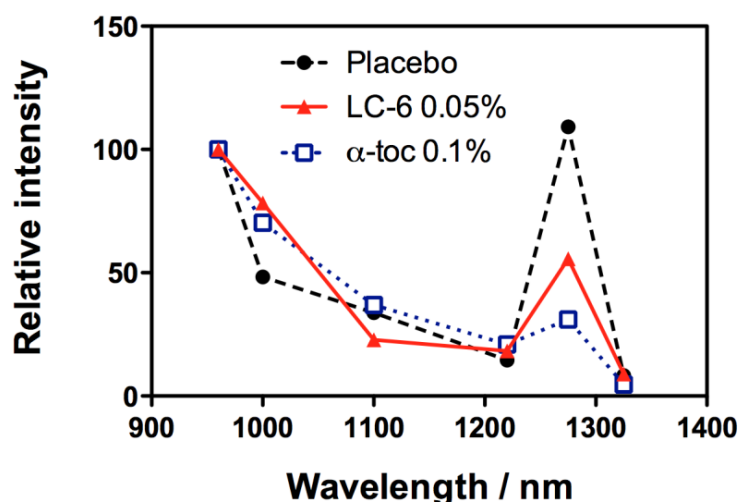
Figure 7.8. Spectra of singlet oxygen luminescence at different wavelengths recorded on 355 nm excitation of ex-vivo porcine skin treated with different TPP containing formulations.

Discussion. A variety of methods exist for assessing the ability of an antioxidant to quench $^1O_2$. Techniques such as electron spin resonance (ESR) [66-69], lipid photo-oxidation [70-72], or by the oxygen radical absorbance capacity (ORAC) [73,74] or its variation, the singlet oxygen absorption capacity (SOAC) assay methods [75,76] are often used. However, these methods can lead to considerable errors as $^1O_2$ is not probed directly and unambiguously [77]. Moreover, their application *in vivo* is also limited since some of these probes are either toxic or do not penetrate tissue to a sufficient extent. In this work we have monitored $^1O_2$ quenching by its time-resolved

phosphorescence, which is regarded as the most specific means for reliable $^1O_2$ detection. At present, this work represents the first report of $^1O_2$ quenching activity of an antioxidant in skin.

Tocopherols rank among the most effective $^1O_2$ scavengers (Fig. 7.1B). Thus α-tocopherol quenches $^1O_2$ with a bimolecular rate constant in ethanol equal to 1.22×10^8 M^{-1} s^{-1} [56], remarkably close to the value found for LC-6. The reactivity of tocopherols towards $^1O_2$ correlates well with their biological activity and it has been suggested that one of the functions of vitamin E might be to protect membrane lipids form oxidative damage by $^1O_2$ [78]. To test whether this observation holds in skin, we formulated two concentrations of LC-6, namely 0.01% and 0.05%, and compared them with 0.1% α-tocopherol formulation. A placebo cream without antioxidants was used as negative control.

The luminescence of $^1O_2$ has been detected in porcine skin exposed to UVA radiation without any exogenous PSs added [44,79]. However, the intensity of this signal was too small for the determination of quenching efficacy of antioxidants [15]. Thus an external PS was added in our experiments to obtain phosphorescence signals with the necessary quality. The PN-photosensitised generation of $^1O_2$ in the skin yielded a decay time of 18 ± 2 μs when the placebo cream was applied. This result is very similar to that obtained by Baier *et al.* [79] for lipid solutions (14 ± 2 μs) and agrees with the notion that skin is a complex system containing a variety of constituents such as water, proteins and, specially, lipids. A quenching effect was clearly observed when LC-6 was added to the formulations. The lifetime of $^1O_2$ in skin treated with LC-6 0.05% cream decayed biexponentially with lifetimes of $\tau_{\Delta1} = 5 \pm 2$ μs and $\tau_{\Delta2} = 13 \pm 2$ μs. In contrast, complete quenching of $^1O_2$ generation was observed using α-tocopherol as antioxidant. Since the $^1O_2$ quenching rate constants k_Q are similar for both antioxidants in solution, these results suggest a different localization pattern of LC-6 and α-tocopherol in the different skin compartments.

7.4. CONCLUSIONS

We have demonstrated that the PS is internalized by cells in a 3D system and is not retained by the ECM, though its internalization is radial. Once the PS is inside the cells, the localization studies revealed no significant differences between 2D and 3D systems. In this work, we reported for the first time the kinetics of singlet oxygen in a 3D cellular culture. The time-resolved fluorescence and NIR luminescence measurements provide useful information to interpret and predict the PDT outcome in real tissues. Substantial differences have neither been shown for the singlet oxygen kinetics. Both phenomena occur at cellular level, with minimal influence of the ECM. Nevertheless, it has been demonstrated the lower accessibility or oxygen concentration in 3D cultures. This fact causes a heterogeneous photodynamic response similar to that reported using *in vivo* models. Thus, this system provides a new method by which better adjust light, oxygen and photosensitizer conditions (dosimetry) for further *in vivo* experiments.

This work also represents the first report of $^1O_2$ quenching activity of an antioxidant in skin. We have found that LC-6 is a potent singlet oxygen scavenger, capable of deactivating this reactive oxygen species with a rate constant of $(1.3 \pm 0.1) \times 10^8$ M^{-1}s^{-1}, a value almost identical to that of α-tocopherol. The anti-singlet oxygen activity of LC-6 has also been demonstrated in *ex-vivo* porcine skin samples. However, these skin results differed to some extent to those obtained in solution suggesting a different localization pattern of both antioxidants within the different skin compartments. This fact evidenced the convenience of these new models for better predicting the outcome of singlet oxygen involved processes.

7.5. REFERENCES

[1] J.W. Snyder, E. Skovsen, J.D.C. Lambert, L. Poulsen, P.R. Ogilby. Optical detection of singlet oxygen from single cells, Phys. Chem. Chem. Phys. 8 (2006) 4280-4293.

[2] J. Moan, K. Berg. The photodegradation of porphyrins in cells can be used to estimate the lifetime of singlet oxygen, Photochem. Photobiol. 53 (1991) 549-553.

[3] A. Jimenez-Banzo, M.L. Sagrista, M. Mora, S. Nonell. Kinetics of singlet oxygen photosensitization in human skin fibroblasts, Free Radic. Biol. Med. 44 (2008) 1926-1934.

[4] J. Baier, T. Maisch, M. Maier, M. Landthaler, W. Baeumler. Direct detection of singlet oxygen generated by UVA irradiation in human cells and skin, J. Invest. Dermatol. 127 (2007) 1498-1506.

[5] C. Flors, M.J. Fryer, J. Waring, B. Reeder, U. Bechtold, P.M. Mullineaux, et al. Imaging the production of singlet oxygen in vivo using a new fluorescent sensor, Singlet Oxygen Sensor Green (R), J. Exp. Bot. 57 (2006) 1725-1734.

[6] M. Niedre, M.S. Patterson, B.C. Wilson. Direct near-infrared luminescence detection of singlet oxygen generated by photodynamic therapy in cells in vitro and tissues in vivo, Photochem. Photobiol. 75 (2002) 382-391.

[7] T. Maisch, J. Baier, B. Franz, M. Maier, M. Landthaler, R.M. Szeimies, et al. The role of singlet oxygen and oxygen concentration in photodynamic inactivation of bacteria, Proc. Natl. Acad. Sci. U.S.A. 104 (2007) 7223-7228.

[8] A. Baker, J.R. Kanofsky. Quenching of singlet oxygen by biomolecules from L1210 leukemia cells, Photochem. Photobiol. 55 (1992) 523-528.

[9] S. Hackbarth, J. Schlothauer, A. Preuss, B. Roeder. New insights to primary photodynamic effects - Singlet oxygen kinetics in living cells, J. Photochem. Photobiol. B: Biol. 98 (2010) 173-179.

[10] A. Jimenez-Banzo, X. Ragas, P. Kapusta, S. Nonell. Time-resolved methods in biophysics. 7. Photon counting vs. analog time-resolved singlet oxygen phosphorescence detection, Photochem. Photobiol. Sci. 7 (2008) 1003-1010.

[11] S. Nonell, S.E. Braslavsky. Time-resolved singlet oxygen detection, Methods Enzymol. 319 (2000) 37-49.

[12] J. Schlothauer, S. Hackbarth, B. Roeder. A new benchmark for time-resolved detection of singlet oxygen luminescence - revealing the evolution of lifetime in living cells with low dose illumination, Laser Phys. Lett. 6 (2009) 216-221.

[13] E. Skovsen, J.W. Snyder, J.D.C. Lambert, P.R. Ogilby. Lifetime and diffusion of singlet oxygen in a cell, J. Phys. Chem. B. 109 (2005) 8570-8573.

[14] R.W. Redmond, I.E. Kochevar. Spatially resolved cellular responses to singlet oxygen, Photochem. Photobiol. 82 (2006) 1178-1186.

[15] J.R. Kanofsky. Measurement of Singlet-Oxygen In Vivo: Progress and Pitfalls, Photochem. Photobiol. 87 (2011) 14-17.

[16] M.K. Kuimova, G. Yahioglu, P.R. Ogilby. Singlet oxygen in a cell: spatially dependent lifetimes and quenching rate constants, J. Am. Chem. Soc. 131 (2009) 332-340.

[17] M.T. Jarvi, M.J. Niedre, M.S. Patterson, B.C. Wilson. The Influence of Oxygen Depletion and Photosensitizer Triplet-state Dynamics During Photodynamic Therapy on Accurate Singlet Oxygen Luminescence Monitoring and Analysis of Treatment Dose Response, Photochem. Photobiol. 87 (2011) 223-234.

[18] L.G. Griffith, M.A. Swartz. Capturing complex 3D tissue physiology in vitro, Nat. rev. 7 211.

[19] L.G. Griffith, G. Naughton, L.G. Griffith, G. Naughton. Tissue engineering--current challenges and expanding opportunities, Science 295 1009.

[20] E.J. Suuronen, H. Sheardown, K.D. Newman, C.R. McLaughlin, M. Griffith. Building in vitro models of organs, Int. Rev. Cytol. 244 137.

[21] A. Huygens, D. Huyghe, G. Bormans, A. Verbruggen, A.R. Kamuhabwa, T. Roskams, et al. Accumulation and photocytotoxicity of hypericin and analogs in two- and three-

dimensional cultures of transitional cell carcinoma cells, Photochem. Photobiol. 78 607.

[22] A.I. Minchinton, I.F. Tannock. Drug penetration in solid tumours, Nat. rev. Cancer. 6 (2006) 583.

[23] R. Derda, A. Laromaine, A. Mammoto, S.K.Y. Tang, T. Mammoto, D.E. Ingber, et al. Paper-supported 3D cell culture for tissue-based bioassays, Proc. Natl. Acad. Sci. U.S.A. 106 (2009) 18457.

[24] K.M. Yamada, E. Cukierman. Modeling tissue morphogenesis and cancer in 3D, Cell. 130 601.

[25] S. Zhang, C. Lockshin, A. Herbert, E. Winter, A. Rich. Zuotin, a putative Z-DNA binding protein in Saccharomyces cerevisiae, EMBO J. 11 (1992) 3787.

[26] S. Zhang, T. Holmes, C. Lockshin, A. Rich. Spontaneous assembly of a self-complementary oligopeptide to form a stable macroscopic membrane, Proc. Natl. Acad. Sci.U.S.A. 90 (1993) 3334.

[27] S. Zhang, T.C. Holmes, C.M. DiPersio, R.O. Hynes, X. Su, A. Rich. Self-complementary oligopeptide matrices support mammalian cell attachment, Biomaterials 16 (1995) 1385.

[28] S. Zhang. Peptide self-assembly in functional polymer science and engineering, React. Funct. Polym. 41 (1999) 91-102.

[29] C.E. Semino. Can We Build Artificial Stem Cell Compartments? J. Biomed. Biotech. 2003 (2003) 164-169.

[30] T.C. Holmes, S. de Lacalle, X. Su, G. Liu, A. Rich, S. Zhang. Extensive neurite outgrowth and active synapse formation on self-assembling peptide scaffolds, Proc. Natl. Acad. Sci. U.S.A. 97 (2000) 6728.

[31] J. Kisiday, M. Jin, B. Kurz, H. Hung, C. Semino, S. Zhang, et al. Self-assembling peptide hydrogel fosters chondrocyte extracellular matrix production and cell division: implications for cartilage tissue repair, Proc. Natl. Acad. Sci. U.S.A. 99 (2002) 9996.

[32] C.E. Semino, J.R. Merok, G.G. Crane, G. Panagiotakos, S. Zhang. Functional differentiation of hepatocyte-like spheroid structures from putative liver progenitor cells in three-dimensional peptide scaffolds, Differentiation 71 (2003) 262.

[33] C.E. Semino, J. Kasahara, Y. Hayashi, S. Zhang. Entrapment of migrating hippocampal neural cells in three-dimensional peptide nanofiber scaffold, Tissue Eng. 10 (2004) 643.

[34] E. Garreta, E. Genové, S. Borrós, C.E. Semino. Osteogenic differentiation of mouse embryonic stem cells and mouse embryonic fibroblasts in a three-dimensional self-assembling peptide scaffold, Tissue Eng. 12 (2006) 2215.

[35] E. Genové, S. Schmitmeier, A. Sala, S. Borrós, A. Bader, L.G. Griffith, et al. Functionalized self-assembling peptide hydrogel enhance maintenance of hepatocyte activity in vitro, J. Cell. Mol. Med. 13 (2009) 3387.

[36] L. Quintana, T.F. Muiños, E. Genove, M. Del Mar Olmos, S. Borrós, C.E. Semino. Early tissue patterning recreated by mouse embryonic fibroblasts in a three-dimensional environment, Tissue Eng. 15 (2009) 45.

[37] I.R. Dégano, L. Quintana, M. Vilalta, D. Horna, N. Rubio, S. Borrós, et al. The effect of self-assembling peptide nanofiber scaffolds on mouse embryonic fibroblast implantation and proliferation, Biomaterials 30 (2008) 1156.

[38] W. Xu, S. Jong Hong, S. Jia, Y. Zhao, R.D. Galiano, T.A. Mustoe. Application of a partial-thickness human ex vivo skin culture model in cutaneous wound healing study, Lab. Invest. (2012).

[39] S. Bessou, J.E. Surleve-Bazeille, C. Pain, P. Donatien, A. Taieb. Ex vivo study of skin phototypes, J. Invest. Dermatol. 107 (1996) 684-688.

[40] B. Godin, E. Touitou. Transdermal skin delivery: predictions for humans from in vivo, ex vivo and animal models, Adv. Drug Deliv. Rev. 59 (2007) 1152-1161.

[41] T. Maisch, F. Santarelli, S. Schreml, P. Babilas, R.M. Szeimies. Fluorescence induction of protoporphyrin IX by a new 5-aminolevulinic acid nanoemulsion used for photodynamic therapy in a full-thickness ex vivo skin model, Exp. Dermatol. 19 (2010) e302-5.

[42] T.G. Smijs, J.A. Bouwstra, H.J. Schuitmaker, M. Talebi, S. Pavel. A novel ex vivo skin model to study the susceptibility of the dermatophyte Trichophyton rubrum to photodynamic treatment in different growth phases, J. Antimicrob. Chemother. 59 (2007) 433-440.

[43] J. Regensburger, A. Knak, T. Maisch, M. Landthaler, W. Baumler. Fatty acids and vitamins generate singlet oxygen under UVB irradiation, Exp. Dermatol. 21 (2012) 135-139.

[44] W. Baumler, J. Regensburger, A. Knak, A. Felgentrager, T. Maisch. UVA and endogenous photosensitizers--the detection of singlet oxygen by its luminescence, Photochem. Photobiol. Sci. 11 (2012) 107-117.

[45] M. Dalle Carbonare, M.A. Pathak. Skin photosensitizing agents and the role of reactive oxygen species in photoaging, J. Photochem. Photobiol. B: Biol. 14 (1992) 105-124.

[46] J. Baier, T. Maisch, M. Maier, E. Engel, M. Landthaler, W. Baumler. Singlet oxygen generation by UVA light exposure of endogenous photosensitizers, Biophys. J. 91 (2006) 1452-1459.

[47] A. Dwivedi, S.F. Mujtaba, H.N. Kushwaha, D. Ali, N. Yadav, S.K. Singh, et al. Photosensitizing Mechanism and Identification of Levofloxacin Photoproducts at Ambient UV Radiation, Photochem. Photobiol. (2011).

[48] F. Vargas, T. Zoltan, A.H. Ramirez, T. Cordero, V. Chavez, C. Izzo, et al. Studies of the photooxidant properties of antibacterial fluoroquinolones and their naphthalene derivatives, Pharmazie. 64 (2009) 116-122.

[49] I. Bogdan Allemann, L. Baumann. Antioxidants used in skin care formulations, Skin Therapy Lett. 13 (2008) 5-9.

[50] F. Dreher, H. Maibach. Protective effects of topical antioxidants in humans, Curr. Probl. Dermatol. 29 (2001) 157-164.

[51] J. Buenger, H. Ackermann, A. Jentzsch, A. Mehling, I. Pfitzner, K.A. Reiffen, et al. An interlaboratory comparison of methods used to assess antioxidant potentials, Int. J. Cosmet. Sci. 28 (2006) 135-146.

[52] J. Cebrian, A. Messeguer, R.M. Facino, J.M. Garcia Anton. New anti-RNS and -RCS products for cosmetic treatment, Int. J. Cosmet. Sci. 27 (2005) 271-278.

[53] N. Sanvicens, V. Gomez-Vicente, A. Messeguer, T.G. Cotter. The radical scavenger CR-6 protects SH-SY5Y neuroblastoma cells from oxidative stress-induced apoptosis: effect on survival pathways, J. Neurochem. 98 (2006) 735-747.

[54] J. Irurre Jr, J. Casas, I. Ramos, A. Messeguer. Inhibition of rat liver microsomal lipid peroxidation elicited by 2,2-dimethylchromenes and chromans containing fluorinated moieties resistant to cytochrome P-450 metabolism, Bioorg. Med. Chem. 1 (1993) 219-225.

[55] M. Miranda, M. Muriach, I. Almansa, E. Arnal, A. Messeguer, M. Diaz-Llopis, et al. CR-6 protects glutathione peroxidase activity in experimental diabetes, Free Radic. Biol. Med. 43 (2007) 1494-1498.

[56] K. Ohara, T. Origuchi, K. Kawanishi, S. Nagaoka. Behavior of Singlet Oxygen in Vitamin E Emulsion, Bull. Chem. Soc. Jpn. 81 (2008) 345-347.

[57] C. Schweitzer, Z. Mehrdad, A. Noll, E. Grabner, R. Schmidt. Mechanism of photosensitized generation of singlet oxygen during oxygen quenching of triplet states and the general dependence of the rate constants and efficiencies of 102 formation on sensitizer triplet state energy and oxidation potential, J. Phys. Chem. 107 (2003) 2192-2198.

[58] J.W. Snyder, E. Skovsen, J.D.C. Lambert, P.R. Ogilby. Subcellular, time-resolved studies of singlet oxygen in single cells, J. Am. Chem. Soc. 127 (2005) 14558-14559.

[59] V.S. Chirvony. Primary photoprocesses in cationic 5,10,15,20-meso-tetrakis(4-N-methylpyridiniumyl) porphyrin and its transition metal complexes bound with nucleic acids, J. Porphyrins Phthalocyanines 7 (2003) 766-774.

[60] I.A. Patito, C. Rothmann, Z. Malik. Nuclear transport of photosensitizers during photosensitization and oxidative stress, Biology Cell 93 (2001) 285-291.

[61] A. Ruck, T. Kollner, A. Dietrich, W. Strauss, H. Schneckenburger. Fluorescence formation

during photodynamic therapy in the nucleus incubated with cationic and anionic water-soluble photosensitizers, J. Photochem. Photobiol. B: Biol., 12 (1992) 403-412.

[62] V.M. De Paoli, S.H. De Paoli, L.E. Borissevitch, A.C. Tedesco. Fluorescence lifetime and quantum yield of TMPyPH2 associated with micelles and DNA, J. Alloys Compounds. 344 (2002) 27-31.

[63] J.W. Snyder, J.D.C. Lambert, P.R. Ogilby. 5,10,15,20-tetrakis(N-methyl-4-pyridyl)-21H,23H-porphine (TMPyP) as a sensitizer for singlet oxygen imaging in cells: Characterizing the irradiation-dependent behavior of TMPyP in a single cell, Photochem. Photobiol. 82 (2006) 177-184.

[64] X. Ragàs, M. Agut, S. Nonell. Singlet oxygen in Escherichia coli: New insights for antimicrobial photodynamic therapy, Free Radic. Biol. Med. 49 (2010) 770-776.

[65] F. Wilkinson, W.P. Helman, A.B. Ross. Rate constants for the decay and reactions of the lowest electronically excited singlet state of molecular oxygen in solution. An expanded and revised compilation, J. Phys. Chem. Ref. Data. 24 (1995) 663-1021.

[66] K. Kobayashi, Y. Maehata, Y. Kawamura, M. Kusubata, S. Hattori, K. Tanaka, et al. Direct assessments of the antioxidant effects of the novel collagen peptide on reactive oxygen species using electron spin resonance spectroscopy, J. Pharmacol. Sci. 116 (2011) 97-106.

[67] A. Yoshida, F. Yoshino, M. Tsubata, M. Ikeguchi, T. Nakamura, M.C. Lee. Direct assessment by electron spin resonance spectroscopy of the antioxidant effects of French maritime pine bark extract in the maxillofacial region of hairless mice, J. Clin. Biochem. Nutr. 49 (2011) 79-86.

[68] A. Iannone, C. Rota, S. Bergamini, A. Tomasi, L.M. Canfield. Antioxidant activity of carotenoids: an electron-spin resonance study on beta-carotene and lutein interaction with free radicals generated in a chemical system, J. Biochem. Mol. Toxicol. 12 (1998) 299-304.

[69] T. Ozawa, A. Hanaki, M. Matsuo. Reactions of superoxide ion with tocopherol and its model compounds: correlation between the

physiological activities of tocopherols and the concentration of chromanoxyl-type radicals, Biochem. Int. 6 (1983) 685-692.

[70] A. Osawa, Y. Ishii, N. Sasamura, M. Morita, H. Kasai, T. Maoka, et al. Characterization and antioxidative activities of rare C(50) carotenoids-sarcinaxanthin, sarcinaxanthin monoglucoside, and sarcinaxanthin diglucoside-obtained from Micrococcus yunnanensis, J. Oleo Sci. 59 (2010) 653-659.

[71] D. Pastore, M.N. Laus, D. Tozzi, V. Fogliano, M. Soccio, Z. Flagella. New tool to evaluate a comprehensive antioxidant activity in food extracts: bleaching of 4-nitroso-N,N-dimethylaniline catalyzed by soybean lipoxygenase-1, J. Agric. Food Chem. 57 (2009) 9682-9692.

[72] A. Baghiani, N. Charef, M. Djarmouni, H.A. Saadeh, L. Arrar, M.S. Mubarak. Free radical scanvenging and antioxidant effects of some anthraquinone derivatives, Med. Chem. 7 (2011) 639-644.

[73] E. Niki. Assessment of antioxidant capacity in vitro and in vivo, Free Radic. Biol. Med. 49 (2010) 503-515.

[74] G. Cao, H.M. Alessio, R.G. Cutler. Oxygen-radical absorbance capacity assay for antioxidants, Free Radic. Biol. Med. 14 (1993) 303-311.

[75] K. Aizawa, Y. Iwasaki, A. Ouchi, T. Inakuma, S. Nagaoka, J. Terao, et al. Development of singlet oxygen absorption capacity (SOAC) assay method. 2. Measurements of the SOAC values for carotenoids and food extracts, J. Agric. Food Chem. 59 (2011) 3717-3729.

[76] A. Ouchi, K. Aizawa, Y. Iwasaki, T. Inakuma, J. Terao, S. Nagaoka, et al. Kinetic study of the quenching reaction of singlet oxygen by carotenoids and food extracts in solution. Development of a singlet oxygen absorption capacity (SOAC) assay method, J. Agric. Food Chem. 58 (2010) 9967-9978.

[77] E. Hideg. Detection of free radicals and reactive oxygen species, Methods Mol. Biol. 274 (2004) 249-260.

[78] G.W. Grams, K. Eskins. Dye-sensitized photooxidation of tocopherols. Correlation

between singlet oxygen reactivity and vitamin E activity, Biochemistry. 11 (1972) 606-608.

[79] J. Baier, M. Maier, R. Engl, M. Landthaler, W. Baumler. Time-resolved investigations of singlet oxygen luminescence in water, in phosphatidylcholine, and in aqueous suspensions of phosphatidylcholine or HT29 cells, J. Phys. Chem. B. 109 (2005) 3041-3046.

Chapter 8

General discussion

## Dissertation and perspectives

---

An integrated discussion of the whole work described in the previous chapters and their implications for photodynamic therapy, as well as signal directions of future research in this field are given in this chapter.

8.1. GENERAL DISCUSSION

The work presented along the previous chapters can be considered as an overview through the photosensitizer (PS) and formulation development in photodynamic therapy (PDT) (Fig 8.1).
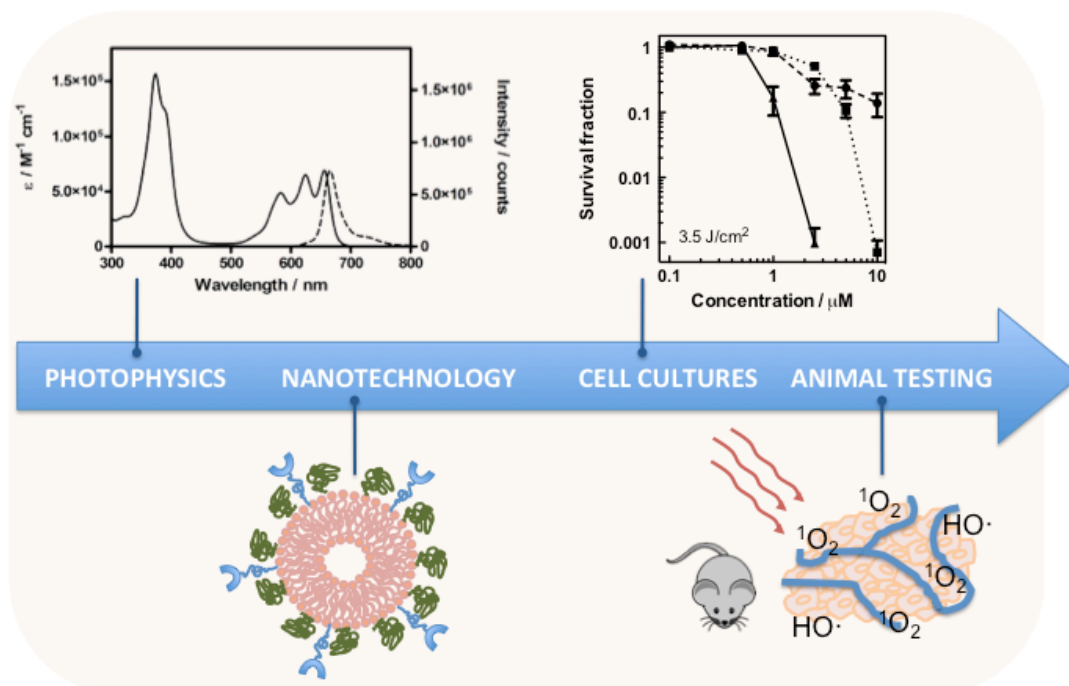
Figure 8.1. Brief overview of the fields studied during this thesis.

The study of photophysical properties of a compound is one of the first filters to validate the goodness of a PS. Owing to the disadvantages presented by Photofrin®, the first drug approved by the Food and Drug Administration (FDA) for PDT purposes, an important effort is being made for the development of new and more efficient PSs, the so-called second generation PSs [1-4]. Amongst these second generation PSs, porphycenes came into focus because their unique properties and features [5-7]. In this work, different strategies have been proposed for improving the design of novel PS based on the porphycene macrocycle. Water-solubility can be achieved by means of the introduction of carboxylate groups in the periphery of the PS core although aggregation is not avoided in this environment and the photophysical properties are

deteriorated even when the porphycene exists in a monomeric state (organic solution). Red shifts in the absorption spectrum and high singlet oxygen formation quantum yields can be attained by introducing heavy-metal ions in the porphycene core. However, most of our efforts have been put into the porphycene analogue to temoporfin, which we call temocene. Temocene shows excellent photophysical properties with high absorption coefficients in the phototherapeutic window (600-800 nm) and a high ability to generate singlet oxygen, although not as high as that of temoporfin [8]. In fact, temocene showed lower photodynamic activity in our first assays delivering it in DMSO to HeLa cells. While these results can be regarded as a disadvantage compared to temoporfin, this could in turn alleviate the skin photosensitivity reported for temoporfin in the few weeks after drug administration [9-11]. Moreover, temocene shows superior photostability than temoporfin and mitochondrial localization. All these results prompted us to study this new photosensitizer further.

Owing to its high hydrophobicity and therefore its poor solubility and aggregation in aqueous solutions, the development of a drug delivery system for *in vitro* and *in vivo* administration of temocene is an unavoidable step. Liposomes were chosen for this purpose due to their unique properties [12,13]. In spite of being one of the most studied carriers for PDT, it is necessary to find the perfect combination of lipids, composition and drug/lipid ratio for each photosensitizer. In the same way that different photosensitizers differ in their photophysical properties, they diverge in their encapsulation requirements. It can be thought that the encapsulation requirements of temoporfin and temocene ought to be comparable as they are structural isomers, but nothing further than reality. Foslip®, the liposomal formulation of temoporfin, is composed of *m*-THPC/DPPC/DPPG (1:11:1.2 molar ratio) [14]. Using these conditions, temocene was encapsulated only poorly. In contrast, we found that the ideal formulation for temocene is *m*-THPPo/DPPC/DMPG (1:67.5:7.5 molar ratio) yielding a high encapsulation efficiency, high drug cargo (16 mM local concentration) and liposome sizes of ca. 120 nm.

The advantages of the encapsulation of temocene in nanocarriers are evidenced in chapter 6, where two different drug delivery systems (liposomes and micelles) were compared with the free drug dissolved in PEG_{400}/EtOH mixture. Lipid based carriers prevent temocene aggregation in aqueous environments, which occurred when delivered in PEG_{400}/EtOH solution. In spite of this fact, the free drug showed the best *in vitro* response because cells were able to internalize the largest amount of PS.

However, the solvent formulation induced an immediate, high and irreversible toxic response when delivered intravenously and had to be ruled out for *in vivo* experiments. Liposomes exhibited the highest killing efficacy per uptaken molecule. A minimal cell internalization and, therefore, no photodynamic activity were observed *in vitro* with the micellar formulation. The subcellular localization of temocene was not affected by the drug-delivery system used and lysosomes were the preferential site of localization in all cases. Only when temocene was dissolved in DMSO mitochondria are the preferential site of accumulation.

In order to minimize the internalization of the drug in normal cells, a folate-targeted liposomal strategy has been proposed. For reasons of synthetic unavailability of temocene, we used the formulation ZnTPP/POPC/OOPS (1:90:10) described in [15] but decorated with folate ligands. This folate-targeted liposomal formulation led 2-fold higher uptake by HeLa cells (folate receptor positive cells) relative to the non-targeted formulation. However, this selectivity was lower than expected as non-specific pathways were also effective for cellular uptake. It is expected that selectivity would be further enhanced in cells with a higher overexpression of folate receptors (e.g. KB cells). Some works have also pointed out the phenomenon so-called "binding site barrier", which considers the idea that macromolecular ligands could be prevented from penetrating tumors by the fact of their successful binding to the target receptor [16]. Considering these drawbacks and the low expectations for the folate-targeted strategy, further *in vivo* studies of temocene activity have been performed only with non-targeted liposomes.

The following stage of the development of a new photosensitizer for PDT is testing its *in vivo* response. Drug delivery systems can also modulate *in vivo* pharmacokinetics, tumor accumulation and photodynamic efficiency. Thus, micellar and liposomal formulations were tested using different targeting strategies (Fig. 8.2).
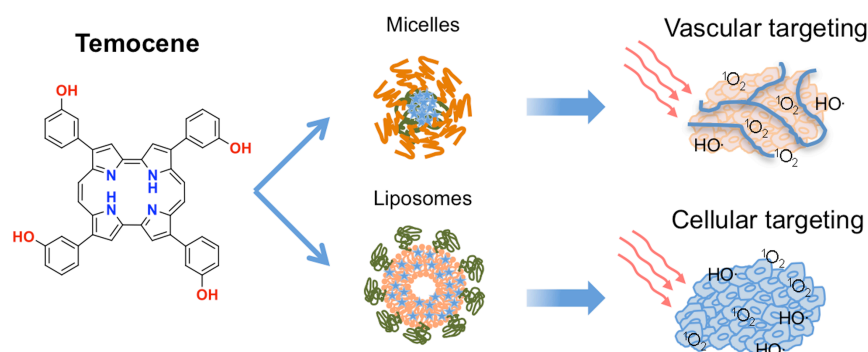
Figure 8.2. Pictorial representation of vascular or cellular targeting strategies followed in this study.

We have shown that both formulation and the time between PS administration and light treatment (targeting strategy) are critical parameters for PDT efficiency. Micellar formulation showed the best *in vivo* response when used in a vascular regimen (short drug-to-light interval), whereas liposomes were found to be an efficient drug delivery system for a tumor cell targeting strategy. Using non-invasive fluorescence techniques we confirmed that pegylated liposomes have a long circulation time showing its maximum tumor accumulation 24 hours post-injection. Compared to micelles, liposomes showed the best tumor selectivity, namely a tumor-to-normal tissue ratio of 3. The aggregation of temocene in the blood stream when dissolved in PEG/EtOH mixture caused the immediate death of the mice, supporting again the importance of drug delivery systems for delivering photosensitizing agents.

It is important to mention that *in vitro* tests not always reproduce the *in vivo* results. Micelles showed no photodynamic activity in 2D-cellular level while they were the most effective formulation for *in vivo* treatments combined with a short drug-to-light interval. This of course reflects that this formulation targets the tumor vasculature, which 2D cultures lack, most likely through a fast temocene exchange with natural carriers present in the bloodstream, such as lipoproteins. In contrast, temocene in PEG/EtOH could be regarded as a good alternative based on the *in vitro* results but failed when it was administered intravenously. These results evidence the necessity of *in vitro* models that better mimic the behavior of tumor tissues and could predict the outcome of vascular and cellular PDT *in vivo.* For this reason, we considered the use of new *in vitro* models for a better optimization of the PDT outcome.

When the studies are subjected to *in vivo* animal trials all the parameters optimized for 2D cultures need to be adjusted again. This step could be avoided or at least minimized using 3D cellular cultures. In this work we reported for the first time the kinetics of singlet oxygen production and decay in a 3D cellular system. The $^1O_2$ behavior is not dramatically affected by the dimensionality of the cellular culture indicating that the production and decay of singlet oxygen are confined cellular phenomena. This result is consistent with our previous studies about the mobility and diffusion of the singlet oxygen inside the cell using ZnTPP as a PS (chapter 5) that concluded that damage of singlet oxygen is confined to the organelle where it is localized. However, a shorter singlet oxygen lifetime was observed, suggesting a

hampered singlet oxygen mobility or quenching by the proteins of the ECM. The triplet lifetime of the PS internalized by cells in the 3D system is also prolonged indicating less accessibility or concentration of oxygen. These results confirm that this model reproduces the oxygen and PS heterogeneity when the extracellular matrix is present and therefore provides useful information to interpret and predict the PDT outcome in real tissues.

Another *in vitro* model commonly used for dermatological issues is the *ex-vivo* porcine skin model. We found that the antioxidant Lipochroman-6, an analog of α-tocopherol, had a different quenching ability in skin relative in solution. Skin is a heterogeneous system and molecules can localize in different compartments depending on their physical properties. These studies supported once again that new *in vitro* cellular models represent an important extension of current testing strategies for drug discovery.

8.2. FUTURE TRENDS

It is more than 25 years since PDT was first used in oncology. Although it is nowadays widely used in some medical specialties, it is more necessary than ever to pursue a continuous research for developing new and better PSs, optimizing their delivery and activation and exploring new therapeutic outcomes.

First-generation PSs exhibited several drawbacks such as prolonged skin photosensitivity and lack of long wavelength absorption. As we have seen, substantial effort has been put into the development of second-generation PSs that present better absorption properties, greater tumor selectivity and shorter periods of photosensitization [1,2]. Future work on the development of PSs is likely to focus on increasing therapeutic efficacy and selectivity for malignant tissue, while minimizing side effects. These third-generation PSs are covalently attached to targeting molecules that have high affinity to receptors expressed in tumor surface such as antibodies, epidermal growth factors or folate ligands [17-20]. Molecular beacons linked to the PS represent another strategy. These molecular beacons quench the PS until the link is cleaved by a specific enzyme of the target site providing not only tumor specificity but also organelle selectivity [21,22]. Organelle selection of damage induced by PDT can also be achieved by means of the genetically encoded PSs that can be expressed only in specific sites of targeted cells [23,24].

An alternative approach is the use of non-linear optical effect of two-photon photodynamic therapy by which the PS simultaneously absorbs two photons of comparatively low energy. Excitation can be confined to a femtoliter volume at the focus therefore it can be exploited to target individual blood vessels. Moreover, the energy of the photons required is comparatively lower than for one-photon excitation and near-infrared light (800-1000 nm) can be used to achieve deeper tissue penetration [25-28]. Our group has previously demonstrated that porphycenes are efficient singlet oxygen two-photon photosensitizers [26].

In this work we have demonstrated that drug delivery systems can modulate and direct PSs to specific targets. Future directions in this field point to the use of multifunctional nanocarriers that act as a "Trojan horse". Ideally, multi-platform drug delivery systems can simultaneously or sequentially accomplish the following set of properties: (1) Specifically target the site of disease by means of different target ligands; (2) Respond local stimuli characteristic of the pathological site such as pH or temperature; (3)

Provide an enhanced intracellular delivery of drugs; (5) Carry a contrast component supplying a real time information about biodistribution and target accumulation [29-32].

Recent times have also seen the emergence of certain promising modalities based on PDT immunotherapy and PDT-based cancer vaccines. It is now accepted that PDT can induce an immune response that assists the complete eradication of tumor and provides a long-term control of tumors [33-36]. In this work, it can be sensed the PDT effect on immune system although it wasn't deeply studied. While it is still in a very early stage, the enhancement of anti-tumor immunity exert by PDT is potentially one of the most significant achievements in the field of PDT.

8.3. REFERENCES

[1] M.J. Garland, C.M. Cassidy, D. Woolfson, R.F. Donnelly. Designing photosensitizers for photodynamic therapy: strategies, challenges and promising developments, Future Med Chem. 1 (2009) 667-691.

[2] A.E. O'Connor, W.M. Gallagher, A.T. Byrne. Porphyrin and nonporphyrin photosensitizers in oncology: preclinical and clinical advances in photodynamic therapy, Photochem. Photobiol. 85 (2009) 1053-1074.

[3] L.B. Josefsen, R.W. Boyle. Photodynamic therapy and the development of metal-based photosensitisers, Metal-based drugs. (2008) 1-24.

[4] S.B. Brown, E.A. Brown, I. Walker. The present and future role of photodynamic therapy in cancer treatment, Lancet Oncol. 5 (2004) 497-508.

[5] E. Vogel, M. Kocher, H. Schmickler, J. Lex. Porphycene - a Novel Porphin Isomer, Angew.Chem.-Int. Edit. Engl. 25 (1986) 257-259.

[6] O. Arad, A. Gavaldà, O. Rey, N. Rubio, D. Sánchez-García, J.I. Borrell, et al. Porphycenes for cancer photochemotherapy and other biomedical applications. Afinidad. 59 (2002) 343-356.

[7] J.C. Stockert, M. Cañete, A. Juarranz, A. Villanueva, R.W. Horobin, J.I. Borrell, et al. Porphycenes: facts and prospects in photodynamic therapy of cancer, Curr. Med. Chem. 14 (2007) 997-1026.

[8] R. Bonnett, P. Charlesworth, B.D. Djelal, J. Foley, D.J. McGarvey, T.G. Truscott. Photophysical properties of 5,10,15,20-tetrakis(m-hydroxyphenyl)-porphyrin (m-THPP), 5,50,15,20-tetrakis(m-hydroxyphenyl)chlorin (m-THPC) and 5,10,15,20-tetrakis(m-hydroxyphenyl)bacteriochlorin (m-THPBC): a comparative study, J. Chem. Soc. Perkin Trans. 2 (1999) 325-328.

[9] A.M. Ronn, M. Nouri, L.A. Lofgren, B.M. Steinberg, A. Westerborn, T. Windahl, et al. Human tissue levels and plasma pharmacokinetics of temoporfin (Foscan®, mTHPC), Lasers Med. Sci. 11 (1996) 267-272.

[10] R.K. Pandey. Recent advances in photodynamic therapy, J. Porphyrins Phthalocyanines 4 (2000) 368-373.

[11] M.O. Senge, J.C. Brandt. Temoporfin (Foscan®, 5,10,15,20-tetra(m-hydroxyphenyl)chlorin)--a second-generation photosensitizer, Photochem. Photobiol. 87 (2011) 1240-1296.

[12] C.S. Jin, G. Zheng. Liposomal nanostructures for photosensitizer delivery, Lasers Surg. Med. 43 (2011) 734-748.

[13] A.S.L. Derycke, P.A.M.d. Witte. Liposomes for photodynamic therapy, Adv. Drug Deliv. Rev. 56 (2004) 17-30.

[14] V. Albrecht, A. Fahr, D. Scheglmann, S. Gräfe, W. Neuberger. Liposomal formulations of hydrophobic photosensitizer for photodynamic therapy, (2008) US7354599.

[15] F. Postigo, M. Mora, M.A. De Madariaga, S. Nonell, M.L. Sagrista. Incorporation of hydrophobic porphyrins into liposomes: characterization and structural requirements, Int. J. Pharm. 278 (2004) 239-254.

[16] J.N. Weinstein, W. van Osdol. Early intervention in cancer using monoclonal antibodies and other biological ligands: micropharmacology and the "binding site barrier", Cancer Res. 52 (1992) 2747s-2751s.

[17] R. Hudson, R.W. Boyle. Strategies for selective delivery of photodynamic sensitisers to biological targets, J. Porphyrins Phthalocyanines. 8 (2004) 954-975.

[18] A.J. Bullous, C.M. Alonso, R.W. Boyle. Photosensitiser-antibody conjugates for photodynamic therapy, Photochem. Photobiol. Sci. 10 (2011) 721-750.

[19] W.M. Sharman, J.E.V. Lier, C.M. Allen. Targeted photodynamic therapy via receptor mediated delivery systems, Adv. Drug Deliv. Rev. 56 (2004) 53-76.

[20] R. Schneider, F. Schmitt, C. Frochot, Y. Fort, N. Lourette, F. Guillemin, et al. Desing, synthesis, and biological evaluation of folic acid

targeted tetraphenylporphyrin as novel photosensitizers for selective photodynamic therapy, Bioorg. Med. Chem. 13 (2005) 2799-2808.

[21] J. Chen, K. Stefflova, M.J. Niedre, B.C. Wilson, B. Chance, J.D. Glickson, et al. Protease-triggered photosensitizing beacon based on singlet oxygen quenching and activation, J. Am. Chem. Soc. 126 (2004) 11450-11451.

[22] G. Zheng, J. Chen, K. Stefflova, M. Jarvi, H. Li, B.C. Wilson. Photodynamic molecular beacon as an activatable photosensitizer based on protease-controlled singlet oxygen quenching and activation, Proc. Natl. Acad. Sci. U.S.A. 104 (2007) 8989-8994.

[23] M.E. Bulina, D.M. Chudakov, O.V. Britanova, Y.G. Yanushevich, D.B. Staroverov, T.V. Chepurnykh, et al. A genetically encoded photosensitizer, Nat. Biotechnol. 24 (2006) 95-99.

[24] S. Pletnev, N.G. Gurskaya, N.V. Pletneva, K.A. Lukyanov, D.M. Chudakov, V.I. Martynov, et al. Structural basis for phototoxicity of the genetically encoded photosensitizer KillerRed, J. Biol. Chem. 284 (2009) 32028-32039.

[25] B.W. Pedersen, T. Breitenbach, R.W. Redmond, P.R. Ogilby. Two-photon irradiation of an intracellular singlet oxygen photosensitizer: achieving localized sub-cellular excitation in spatially-resolved experiments, Free Radic. Res. 44 (2010) 1383-1397.

[26] J. Arnbjerg, A. Jimenez-Banzo, M.J. Paterson, S. Nonell, J.I. Borrell, O. Christiansen, et al. Two-photon absorption in tetraphenylporphycenes: are porphycenes better candidates than porphyrins for providing optimal optical properties for two-photon photodynamic therapy? J. Am. Chem. Soc. 129 (2007) 5188-5199.

[27] J. Arnbjerg, M. Johnsen, P.K. Frederiksen, S.E. Braslavsky, P.R. Ogilby. Two-photon photosensitized production of singlet oxygen: optical and optoacoustic characterization of absolute two-photon absorption cross sections for standard sensitizers in different solvents, J. Phys. Chem. A 110 (2006) 7375-7385.

[28] H.A. Collins, M. Khurana, E.H. Moriyama, A. Mariampillai, E. Dahlstedt, M. Balaz, et al. Blood-vessel closure using photosensitizers engineered for two-photon excitation, Nat. Photon. 2 (2008) 420-424.

[29] V. Torchilin. Multifunctional and stimuli-sensitive pharmaceutical nanocarriers, Eur. J. Pharm. Biopharm. 71 (2009) 431-444.

[30] R.R. Sawant, V.P. Torchilin. Liposomes as 'smart' pharmaceutical nanocarriers, Soft Matter. 6 (2010) 4026-4044.

[31] V.P. Torchilin. Multifunctional nanocarriers, Adv. Drug Deliv. Rev. 58 (2006) 1532-1555.

[32] D. Needham, M.W. Dewhirst. The development and testing of a new temperature-sensitive drug delivery system for the treatment of solid tumors, Adv. Drug Deliv. Rev. 53 (2001) 285-305.

[33] A.D. Garg, D. Nowis, J. Golab, P. Agostinis. Photodynamic therapy: illuminating the road from cell death towards anti-tumour immunity, Apoptosis. 15 (2010) 1050-1071.

[34] A.D. Garg, D.V. Krysko, P. Vandenabeele, P. Agostinis. DAMPs and PDT-mediated photo-oxidative stress: exploring the unknown, Photochem. Photobiol. Sci. 10 (2011) 670-680.

[35] M. Korbelik. Cancer vaccines generated by photodynamic therapy, Photochem. Photobiol. Sci. 10 (2011) 664-669.

[36] S.O. Gollnick, C.M. Brackett. Enhancement of anti-tumor immunity by photodynamic therapy, Immunol. Res. 46 (2010) 216-226.

Chapter 9
Conclusions

1. Temocene (*m*-THPPo), the porphycene analogue of temoporfin, shows 2.5-fold larger absorption coefficients than this approved photosensitizer in the red part of the spectrum, as well as higher photostability and lower dark toxicity. However its photodynamic activity towards HeLa cancer cells is lower.

2. Palladium(II) coordination of 2,7,12,17-tetraphenylporphycene (TPPo) hampers its liposomal encapsulation. Highly unsaturated lipids and high drug-to-lipid molar ratios are needed making the liposomal formulation toxic by itself.

3. A liposomal formulation of temocene (*m*-THPPo/DPPC/DMPG with 1:67.5:7.5 molar ratio), has been developed that yields liposomes of size 120 ± 40 nm with high encapsulation efficiency and high drug payload. The photophysical properties and singlet oxygen production ability of porphycene remain close to those in solution.

4. Folate targeting of liposomes incorporating the model photosensitizer Zn(II)-*meso*-tetraphenylporphine leads to a 2-fold higher uptake than the corresponding non-targeted liposomal formulation.

5. Three delivery systems, namely the solvent mixture propyleneglycol:ethanol, Cremophor EL micelles, and DPPC/DMPG/PEG$_{3000}$-DSPE liposomes were compared as vehicles for temocene in antitumour photodynamic therapy *in vivo*. The solvent mixture led to high toxicity. Micellar formulation showed the best *in vivo* response when used in a vascular regimen (short drug-to-light interval), whereas liposomes were the best drug delivery system for a tumor cell targeting strategy, showing a tumor-to-normal tissue selectivity ratio of 3.

6. The subcellular distribution of the photosensitizer *meso*-tetrakis(4-*N*-methylpyridylium)porphyrin in three-dimensional cell cultures is the same as in conventional 2D cultures. The kinetics of singlet oxygen production and decay in 3D cultures revealed lower oxygen accessibility to the photosensitizer.

7. Lipochroman-6 is able to quench the production of singlet oxygen in an *ex-vivo* porcine skin model although is less efficient than α-tocopherol.

LIST of ABBREVATIONS

ALA	5-aminolevulinic acid
AMD	age-related macular degeneration
AP	antioxidative power
BCA	bicinchoninic acid
BHT	3,5-di-tert-butyl-4-hydroxytoluene
BSA	bovine serum albumin
CAM	chick chorioallantoic membrane
CV	cresyl violet
DIC	differential interference contrast
DMEM	Dulbecco´s Modified Eagle´s Medium
DMPC	1,2-dimyristoyl-*sn*-glycero-3-phosphocholine
DMPG	1,2-dimyristoyl-*sn*-glycero-3-phospho-(1'-rac-glycerol)
DMSO	dimethyl sulfoxide
DNA	deoxyribonucleic acid
D-PBS	deuterated phosphate-buffered saline
DPPC	1,2-dipalmitoyl-*sn*-glycero-3-phosphocholine
DPPG	1,2-dipalmitoyl-*sn*-glycero-3-phospho-(1'-rac-glycerol)
DSPC	1,2-distearoyl-*sn*-glycero-3-phosphocholine
DSPG	1,2-distearoyl-*sn*-glycero-3-phospho-(1'-rac-glycerol)
ECM	extracellular matrix
EPR	enhanced permeability and retention effect
ER	endoplasmic reticulum
ESR	electron spin resonance
FA-PEG-DSPE	2-distearoyl-*sn*-glycero-3-phosphoethanolamine-N [folate(polyethylene glycol)-2000] (ammonium salt)
FBS	fetal bovine serum
Φ_Δ	singlet oxygen quantum yield
FD-DMEM	folate-deficient Dulbecco´s Modified Eagle´s Medium
Φ_F	fluorescence quantum yield
FR	folate receptor
GPx	glutathione peroxidase
hNDF	normal human dermal fibroblasts
HPF	3'-(p-hydroxyphenyl) fluorescein
HPLC	high performance liquid chromatography
H&E	hematoxylin and eosin

IPA	image processing and analysis
iPrOTPPo	2,7,12,17-(3-carboxyphenyl) porphycene
IR	infrared radiation
IRF	instrument's response function
LC-6	lipochroman-6
LED	light emitting diode
MDA	malondialdehyde
MLV	multilamellar vesicle
m-PEG$_{3000}$-DSPE	1,2-distearoyl-sn-glycero-3-phosphoethanolamine-N-[methoxy(polyethylene glycol)-3000]
m-TCPPo	2,7,12,17-(3-carboxyphenyl) porphycene
m-THPPo	2,7,12,17-(3-hydroxyphenyl) porphycene
MTT	3-[4,5-dimethylthiazol-2-yl]-2,5-diphenyltetrazolium bromide
NADH/NAD	nicotinamide adenine dinucleotide
NIH	national institutes of health
NIR	near infrared radiation
NP	nanoparticle
$^1O_2$	singlet oxygen
OOPS	1,2-dioleoyl-sn-glycero-3-[phospho-L-serine] (sodium salt)
ORAC	oxygen radical absorption capacity
PBS	phosphate-buffered saline
PCS	photon correlation spectroscopy
PDT	photodynamic therapy
PdTHPPo	Pd(II)-2,7,12,17-(3-hydroxyphenyl) porphycene
PdTPPo	Pd(II)-2,7,12,17-tetraphenyl porphycene
PEG	polyethylene glycol
PN	1H-phenalen-1-one
POPC	1-palmitoyl-2-oleoyl-sn-glycero-3-phosphocholine
PS	photosensitizer
^3PS	triplet excited state of photosensitizer
RCS	reactive carbonyl species
RES	reticuloendothelial system
RNS	reactive nitrogen species
ROS	reactive oxygen species
RPMI	Roswell Park Memorial Institute
SDS	sodium dodecyl sulfate
SOAC	singlet oxygen absorption capacity

SOSG	singlet oxygen sensor green
Soy-PC	soy extract phosphatidylcholine
TBA	2-thiobarbituric acid
TBARS	thiobarbituric acid reactive species
TCSPC	time correlated single photon counting
$\boldsymbol{\tau}_\Delta$	singlet oxygen lifetime
THF	tetrahydrofuran
$\mathbf{T_m}$	phase transition temperature
TMPyP	5,10,15,20-tetrakis(*N*-methyl-4-pyridil)-21*H*,23*H*-porphine
TPP	5,10,15,20-tetraphenyl-21*H,23H*-porphine
TPPo	2,7,12,17-tetraphenyl porphycene
TRPD	time-resolved NIR phosphorescence detection
$\boldsymbol{\tau_T}$	triplet lifetime
UV	ultraviolet radiation
Vis	visible
ZnTPP	5,10,15,20-tetraphenyl-21*H*,23*H*-porphine zinc